Allocating Classes for Soft-Then-Hard Subpixel Mapping Algorithms in Units of Class

Qunming Wang, Wenzhong Shi, and Liguo Wang

Abstract—There is a type of algorithm for subpixel mapping (SPM), namely, the soft-then-hard SPM (STHSPM) algorithm that first estimates soft attribute values for land cover classes at the subpixel scale level and then allocates classes (i.e., hard attribute values) for subpixels according to the soft attribute values. This paper presents a novel class allocation approach for STHSPM algorithms, which allocates classes in units of class (UOC). First, a visiting order for all classes is predetermined, and the number of subpixels belonging to each class is calculated using coarse fraction data. Then, according to the visiting order, the subpixels belonging to the being visited class are determined by comparing the soft attribute values of this class, and the remaining subpixels are used for the allocation of the next class. The process is terminated when each subpixel is allocated to a class. UOC was tested on three remote sensing images with five STHSPM algorithms: backpropagation neural network, Hopfield neural network, subpixel/pixel spatial attraction model, kriging, and indicator cokriging. UOC was also compared with three existing allocation methods, i.e., linear optimization technique (LOT), sequential assignment in units of subpixel (UOS), and a method that assigns subpixels with highest soft attribute values first (HAVF). Results show that for all STHSPM algorithms, UOC is able to produce higher SPM accuracy than UOS and HAVF; compared with LOT, UOC is able to achieve at least comparable accuracy but needs much less computing time. Hence, UOC provides an effective and real-time class allocation method for STHSPM algorithms.

Index Terms—Class allocation, image classification, subpixel mapping (SPM), subpixel sharpening, superresolution mapping.

I. INTRODUCTION

LAND cover is a critical variable that impacts on many parts of the human and physical environments [1]. Land cover information in remote sensing images is usually extracted by land cover classification. Due to the widely existed mixed pixels, some techniques have been developed to extract information that is smaller than a pixel, including endmember

Q. Wang is with the Department of Land Surveying and Geo-Informatics, The Hong Kong Polytechnic University, Kowloon, Hong Kong (e-mail: wqm11111@126.com).

W. Shi is with the Department of Land Surveying and Geo-Informatics, The Hong Kong Polytechnic University, Kowloon, Hong Kong, and also with Wuhan University, Wuhan 430072, China (e-mail: lswzshi@polyu.edu.hk).

L. Wang is with the College of Information and Communications Engineering, Harbin Engineering University, Harbin 150001, China (e-mail: wangliguo@hrbeu.edu.cn).
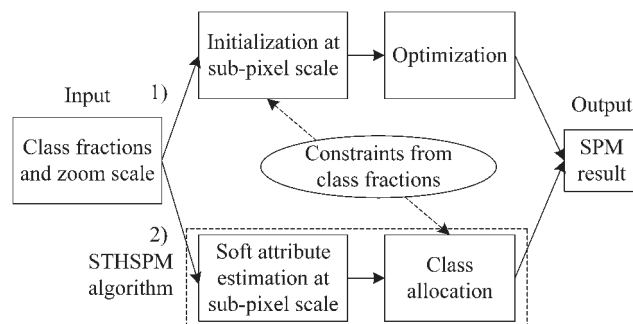
Fig. 1. Two types of SPM algorithms, where "constraints from class fractions" means the class fractions are used to determine the number of subpixels for each class.

extraction [2], soft classification [3], and subpixel mapping [4] (SPM, also termed superresolution mapping [5], [6]) that determine the land cover classes contained within a mixed pixel, the proportions or fractions of the classes, and their spatial distribution, respectively. According to the outputs of soft classification (i.e., fractions of classes) and desired zoom scale, the number of subpixels belonging to each class can be determined, and the aim of SPM is to predict the spatial location of subpixels for each class. SPM is essentially a hard classification technique at a finer spatial resolution than that of the input coarse spatial resolution remote sensing image.

SPM has been paid increasing attention these years, and various SPM algorithms have been developed. In terms of the way of obtaining the SPM results, there are two basic types of SPM algorithms (see Fig. 1).

1) For the first type, the subpixels for each class are first allocated randomly (or by using some fast SPM algorithms [7]–[9]) under the condition of maintaining class fractions. Then, the initialized subpixel map is optimized by changing the spatial arrangement of subpixels inside coarse pixels to gradually approach a certain objective, such as maximizing the attraction between neighboring subpixels in pixel-swapping algorithm [7], [10], [11], the neighboring value [12], [13], the Moran's I of the image [14], simultaneously the attractions between and within pixels [8], or minimizing the perimeter of the area belonging to each class [15]. In addition, the objective of optimization can be to match the two-point histogram [16], [17] or landscape structure [18] extracted from training images. The optimization can be realized by employing artificial intelligence algorithms to solve the relevant models, including particle swarm optimization in [7], simulating annealing in [14]–[16] and [18], and genetic algorithms in [8] and [12]. During the

optimization process, only the spatial locations of the subpixels can vary, and the number of subpixels for each class within each coarse pixel is fixed.

2) The second type of SPM algorithm consists of two steps. First, the soft attribute values (between 0 and 1) of all classes for all subpixels are estimated, and a set of soft-classified images for all classes at a desired fine spatial resolution are generated in this way. This step is also termed subpixel sharpening [19]. The second step is to allocate hard attribute values for subpixels according to the soft attribute values of each class and constraints from class fractions. Algorithms falling into this type include subpixel/pixel spatial attraction model (SPSAM) [20], back-propagation neural network (BPNN) [19], [21]–[23], Hopfield neural network (HNN) [24]–[27], kriging [28], and indicator cokriging (ICK) [29]–[32]. To facilitate description in the whole paper, we denote this type of SPM algorithm as soft-then-hard SPM (STHSPM) algorithm. For both BPNN and ICK, prior spatial structure information at fine spatial resolution is needed, in order to train the network and extract the semivariance, respectively. HNN requires a large number of iterations to minimize the energy function in its model. With respect to SPSAM and kriging, they do not need prior information at fine spatial resolution or iterations to estimate soft attribute values at subpixel scale.

Additionally, [33]–[35] applied an SPM method to directly draw the boundaries of classes according to the coarse fractions, which is different from the previous two types of algorithms. This method, however, does not maintain coarse proportion [33] and may fail to restore land cover objects within a single coarse pixel. SPM can be also performed by the one-stage methods that do not need soft classification process and take as input the raw image in units of reflectance [5], [6], [36], [37]. These methods consider spectral and spatial information simultaneously to achieve SPM. The estimation of the parameter controlling the contributions from spatial and spectral terms is always a case-by-case problem: the choice of the optimum parameter depends upon the spatial pattern of studied area and spectral variation of the remote sensing image.

In recent years, the two types of SPM algorithms in Fig. 1 have been extended and enhanced by making use of various additional information, such as using LIDAR data [38], intermediate spatial resolution fused images [39], subpixel shifted remote sensing images [40], [41], panchromatic images [42] for HNN, fine scale information for ICK [43], panchromatic images for two-point histogram [16], digital elevation models [44], and shape information [45] for pixel-swapping algorithm.

How to allocate classes for STHSPM algorithms is a critical issue that directly affects the performance of STHSPM and needs in-depth study. When HNN-based SPM was initially proposed, a simple class allocation approach was applied: each subpixel is assigned to the class with the highest soft attribute value. This approach is easy to realize, since it does not take the constraints from class fractions into account and is carried out by only comparing the soft attribute values for subpixel. The approach was also applied to some other STHSPM algorithms, such as BPNN in [19] and [21]–[23] and ICK in [43]. However, the experiments in the related literature showed that this allocation approach does not guarantee coarse proportion

reproduction and the SPM results are over smooth. It is insufficient to reproduce land cover objects smaller than a coarse pixel [41].

In [28], linear optimization technique (LOT) was introduced to allocate class. In that work, kriging was applied to estimate the soft attribute value for each class at each location. A mathematical model was then constructed to maximize the sum of soft attribute values of all subpixels in SPM results, while satisfying constraints from class fractions. The model was solved using LOT. LOT can obtain the theoretically optimal solution in terms of maximizing the objective function in the mathematical model. However, LOT involves numbers of iterations to gradually approach the optimal solution. When the zoom scale or the number of classes is large, much time will be consumed. Computational burden is a key issue in the LOT-based class allocation method [28].

A sequential-assignment-based class allocation method was also adopted for class allocation in [29]–[31]. It assigns classes in units of subpixel (UOS). With UOS, the hard-classified subpixel map is generated along a randomly predefined path that determines the order of visited subpixels. According to the path, each visited subpixel is assigned to the class with the highest soft attribute value, on condition that the subpixels of the dominant class have not been completely exhausted. In this way, the subpixel class labels within coarse pixels reproduce exactly the corresponding coarse fractions. The UOS method involves no iteration and is fast. However, many speckle artifacts appear in SPM results when UOS is used [31].

Another sequential-assignment-based class allocation method was applied in [19], [20], and [32], where subpixels with highest soft attribute values are assigned first (HAVF). With the HAVF-based method, among soft attribute values for all subpixels and all classes within each coarse pixel, the highest one is found out during each comparison, and the corresponding subpixel of this value is allocated to the dominant class if the subpixels of this class have not been completely exhausted. The main difference between HAVF and UOS is that the visiting order of subpixels in HAVF is not randomly determined, instead, each subpixel in the path is specified by comparison of all soft attribute values.

In this paper, a novel sequential-assignment-based class allocation method is proposed for STHSPM algorithms, which allocates classes in units of class (UOC). Unlike UOS and HAVF, UOC allocates classes for subpixels along a predefined path that determines the order of visited class. The visiting order of all classes can be obtained from Moran's I [14], an index of intraclass spatial correlation. The proposed UOC approach holds several characteristics and advantages.

1) Similar to UOS and HAVF, UOC is free of any iteration. UOC is a very fast method (particularly in comparison with LOT).
2) Similar to LOT, UOS, and HAVF, UOC is implemented under the condition of reproducing exactly the coarse fraction data.
3) The unique advantage of UOC over LOT, UOS, and HAVF is that UOC is processed on each soft-classified image at fine spatial resolution in turn. In STHSPM algorithms, intraclass spatial dependence is taken into consideration in the first step. As a result, within each coarse pixel, subpixels staying together tend to have

close soft attribute values for the same class, and each generated soft-classified image at fine spatial resolution encapsulates intraclass spatial correlation. During class allocation in UOC, autocorrelation for each class can be maximized, and hence, the proposed method is able to produce more satisfactory SPM results.

The contributions of this paper are given as follows.

1) STHSPM algorithms are introduced, and five STHSPM algorithms (i.e., BPNN, HNN, SPSAM, kriging, and ICK) are systematically summarized for the first time.
2) Existing class allocation methods (i.e., LOT, UOS, and HAVF) for STHSPM algorithms are systematically summarized for the first time.
3) Proposing a new class allocation method, i.e., UOC, for STHSPM algorithms.
4) Proposing an approach to estimate Moran's I from coarse fraction images to determine the visiting order of classes in UOC, which needs no prior class information.
5) Intercomparison of the five STHSPM algorithms is studied.

The rest of this paper is organized as follows: In Section II, the five STHSPM algorithms, i.e., BPNN, HNN, SPSAM, kriging, and ICK, are briefly described. Section III introduces three existing class allocation methods, i.e., LOT, UOS, and HAVF. Section IV presents details of the proposed UOC, including implementation steps of UOC and using Moran's I to specify the visiting order of classes. Experimental results are provided and discussed in Section V, and conclusions are drawn in Section VI.

II. STHSPM ALGORITHMS

As mentioned in the introduction, STHSPM algorithms contain two steps: 1) subpixel sharpening: computing soft attribute values for each class at fine pixels and 2) class allocation: allocating classes for these fine pixels according to the soft attribute values and class fractions. The outputs of the first and second steps are a set of soft-classified images and a set of hard-classified images for all classes at fine spatial resolution, respectively. The first step can be accomplished by BPNN, HNN, SPSAM, kriging, and ICK. The first steps of these five STHSPM algorithms are briefly introduced in this section.

Suppose S is the zoom scale factor (i.e., each coarse pixel is divided into S^2 subpixels), P_t ($t = 1, 2, \ldots, M$; M is the number of pixels in the coarse image) is a coarse pixel, p_i ($i = 1, 2, \ldots, MS^2$) is a subpixel, and $Z_k(p_i)$ denotes the soft attribute value for the kth ($k = 1, 2, \ldots, K$; K is the number of classes) class at subpixel p_i. The outputs of the first step of STHSPM algorithm are $\{Z_k(p_i)|i = 1, 2, \ldots, MS^2; k = 1, 2, \ldots, K\}$. Define $x_k(p_i)$ as the binary class indicator for the kth class at subpixel p_i

$$x_k(p_i) = \begin{cases} 1, & \text{if subpixel } p_i \text{ belongs to class } k \\ 0, & \text{otherwise.} \end{cases} \quad (1)$$

A. BPNN-Based SPM

References [19] and [21]–[23] presented a BPNN-based SPM method. This method first extracts training samples from available high spatial resolution images, which are used as training images. The input of each training sample is a vector composed of coarse fractions for the kth class at all coarse pixels within a local window, whereas the output is a vector composed of $x_k(p_i)$ for all subpixels within the center coarse pixel. The training samples are then used to fit a BPNN. During the training process, the connection weightings between neurons of different layers are obtained iteratively. The trained BPNN is used to predict the outputs of test samples subsequently, of which the inputs are extracted from the fraction images for SPM.

B. HNN-Based SPM

In HNN-based SPM, each subpixel is considered as a neuron, and HNN is set up to minimize an energy function that comprises a goal and constraints [10], [24]–[27], i.e.,

$$E = \alpha_1 G + \alpha_2 C \quad (2)$$

where α_1 and α_2 are weightings, the term G is to increase the spatial correlation between neighboring subpixels, and C are the constraints from the fraction data and the sum-to-one condition (i.e., the sum of soft attribute values for all classes at each neuron is equal to 1) [24]–[27]. The HNN is an optimization tool in nature. In this model, the attribute value (between 0 and 1) per subpixel per class is pushed iteratively toward 0 or 1 [46]. The output of each neuron, i.e., $Z_k(p_i)$, is an attribute value either close to 0 or 1, but not completely equal to 0 or 1.

C. SPSAM-Based SPM

Mertens *et al.* [20] applied SPSAM to directly calculate the spatial correlation between subpixels and their neighboring pixels by attractions. Suppose the neighboring coarse pixels of subpixel p_i are $P_1, P_2, \ldots, P_N$ (N is the number of neighboring coarse pixels). In SPSAM, each p_i is assumed to be attracted by its neighboring coarse pixels. The soft attribute value $Z_k(p_i)$ can be calculated by the attraction from the kth class to p_i, i.e.,

$$Z_k(p_i) = \frac{1}{N} \sum_{n=1}^{N} \frac{F_k(P_n)}{d(P_n, P_i)} \quad (3)$$

where $d(P_n, p_i)$ is the Euclidean distance between geometric centers of pixel P_n and subpixel p_i, and $F_k(P_n)$ is the coarse fraction of the kth class at the nth neighboring pixel P_n.

D. Kriging-Based SPM

The kriging-based SPM developed by [28] was based on the assumption that the soft attribute value for each class at each location (i.e., subpixel) is a weighted linear combination of N_0 observed values, i.e.,

$$Z_k(p_i) = \sum_{n=1}^{N_0} \beta_n Z_k(P_n) \quad (4)$$

where β_n is a weight, and $Z_k(P_n)$ denotes a continuous variable for the kth class at pixel P_n. $Z_k(P_n)$ can be depicted by fraction of the kth class at P_k, and β_n are estimated by solving the kriging system [47]. The semivariance in the kriging system

can be derived from the coarse images, which does not require any prior information.

E. ICK-Based SPM

Let all fractions for the kth class be arranged in a $(M \times 1)$ vector $\mathbf{F}_k$ and π_k be the mean of all elements in vector $\mathbf{F}_k$. Suppose there are H informed (i.e., the class labels are known) fine pixels available and the H indicators for the kth class are arranged in a $(H \times 1)$ vector $\mathbf{j}_k$. Then, the soft attribute value $Z_k(p_i)$ can be estimated by

$$Z_k(p_i) = \boldsymbol{\eta}_k(p_i)^T \mathbf{F}_k + \boldsymbol{\lambda}_k(p_i)^T \mathbf{j}_k +$$
$$\pi_k \left[1 - sum\left(\boldsymbol{\eta}_k(p_i)^T\right) - sum\left(\boldsymbol{\lambda}_k(p_i)^T\right) \right] \quad (5)$$

where the $(M \times 1)$ vector $\boldsymbol{\eta}_k(p_i)$ and the $(H \times 1)$ vector $\boldsymbol{\lambda}_k(p_i)$ are ICK weightings for the kth class. The function $sum(\bullet)$ takes the sums of all the elements in vector $\bullet$. The weightings $\boldsymbol{\eta}_k(p_i)$ and $\boldsymbol{\lambda}_k(p_i)$ are calculated by solving the ICK system [29]–[32]. The semivariance in the ICK system needs to be extracted from available fine spatial resolution images.

The soft attribute value $Z_k(p_i)$ estimated by STHSPM algorithms can be understood as the probability of the kth class occurrence at subpixel p_i. Usually, the preliminarily obtained soft attribute value, denoted as $Z'_k(p_i)$, may be less than 0 or may not satisfy the sum-to-one condition (particularly for BPNN). Taking account of the physical meaning, two extra steps for adjustments are applied. The first is to revise the attribute values to 0 if they are less than 0, and the second is to normalize the soft attribute values by

$$Z_k(p_i) = \frac{Z'_k(p_i)}{\sum\limits_{k=1}^{K} Z'_k(p_i)} \quad (6)$$

so that $Z_k(p_i) \in [0, 1]$ and $\sum_{k=1}^{K} Z_k(p_i) = 1$.

III. THREE CLASS ALLOCATION METHODS FOR STHSPM ALGORITHMS

The ultimate goal of SPM is to generate hard-classified maps at the subpixel level. After $\{Z_k(p_i) | i = 1, 2, \ldots, MS^2; \ k = 1, 2, \ldots, K\}$ are obtained by any STHSPM algorithm introduced in Section II, they are used to allocate hard attribute values for subpixels along with the class fractions. This section describes three existing class allocation methods, i.e., LOT, UOS, and HAVF.

To facilitate description in this section, all subpixels in the coarse image that has M pixels are divided into M groups, i.e., $\{p_i | i = 1, 2, \ldots, MS^2\}$ is re-denoted as $\{p_i^t | i = 1, 2, \ldots, S^2; \ t = 1, 2, \ldots, M\}$, where p_i^t denote the subpixels within coarse pixel P_t, and S is the zoom scale factor. The objective of class allocation is to acquire binary class indicators $\{x_k(p_i^t) | i = 1, 2, \ldots, S^2; \ t = 1, 2, \ldots, M; \ k = 1, 2, \ldots, K\}$, and a subpixel map R (i.e., SPM result) having K gray values can be produced by

$$R\left(p_i^t\right) = \sum_{k=1}^{K} k x_k\left(p_i^t\right), \qquad i = 1, 2, \ldots S^2; \ t = 1, 2, \ldots, M. \quad (7)$$

As can be concluded from (1) and the principle that each subpixel belongs to only one class, $R(p_i^t) = 1, 2, \ldots, K$.

A. LOT

LOT was introduced in [28] for kriging-based SPM, which is to maximize an objective function while meeting a set of equality constraints. In the following constructed mathematical model, for each coarse pixel P_t in the coarse image, J_t is maximized:

$$\max \ J_t = \sum_{i=1}^{S^2} \sum_{k=1}^{K} x_k\left(p_i^t\right) Z_k\left(p_i^t\right)$$

$$\text{s.t.} \ \sum_{k=1}^{K} x_k\left(p_i^t\right) = 1, \qquad i = 1, 2, \ldots, S^2$$

$$\sum_{i=1}^{S^2} x_k\left(p_i^t\right) = F_k(P_t)S^2, \qquad k = 1, 2, \ldots, K \quad (8)$$

where $F_k(P_t)$ is the coarse fraction of the kth class at pixel P_t, and $\sum_{k=1}^{K} F_k(P_t) = 1$. $Z_k(p_i^t)$ were originally obtained by kriging in [28], but we know now they can be also calculated by any STHSPM algorithm introduced in Section II. The two types of equality constraints in (8) can be written as the two corresponding expressions

$$\boldsymbol{X}\mathbf{1}_K = \mathbf{1}_{S^2} \quad (9)$$

$$\boldsymbol{X}^T\mathbf{1}_{S^2} = \boldsymbol{S}^2\boldsymbol{F} \quad (10)$$

where $\boldsymbol{X}$ is a $(S^2 \times K)$ matrix

$$\boldsymbol{X} = \begin{bmatrix} x_1\left(p_1^t\right) & x_2\left(p_1^t\right) & \cdots & x_K\left(p_1^t\right) \\ x_1\left(p_2^t\right) & x_2\left(p_2^t\right) & \cdots & x_K\left(p_2^t\right) \\ \cdots & \cdots & \cdots & \cdots \\ x_1\left(p_{S^2}^t\right) & x_2\left(p_{S^2}^t\right) & \cdots & x_K\left(p_{S^2}^t\right) \end{bmatrix}$$

and $\boldsymbol{F} = [F_1(P_t), F_2(P_t), \ldots, F_K(P_t)]^T$. $\mathbf{1}_K$ and $\mathbf{1}_{S^2}$ denote a $(K \times 1)$ and a $(S^2 \times 1)$ vector of ones, respectively.

Constraints in (9) means that each subpixel should be assigned to only one class, whereas constraints in (10) means that the number of subpixels belonging to each class should be consistent with the coarse fraction data. In all, this mathematical model is to maximize the sum of soft attribute values of all subpixels in the resulting SPM map, in the meanwhile, fixing the number of subpixels for each class according to the coarse fractions. The linear problem in (8) can be solved by LOT, and the classical simplex algorithm [48] can be employed for this purpose.

Using LOT, the optimal solution to (8) will be generated. The whole process, however, requires numbers of iterations and is time consuming. It can be observed that, for each coarse pixel, there are KS^2 variables and $K + S^2$ equality constraints in (8), and correspondingly KS^2 elements in matrix X. Therefore, the computing complexity is closely related to M, K, and S. When K or S increases, the computing complexity will noticeably increase. Computational limitations prevent further research into finer spatial resolutions and more classes [28].

B. UOS

The sequential-assignment-based class allocation method, i.e., UOS, is also performed under the conditions of meeting the equality constraints in (8) or (9) and (10), and the basic principle of UOS is the same as the objective function in (8). The class allocation process of UOS, however, is different from LOT. UOS is performed by direct comparison of K soft attribute values for each subpixel.

UOS first determines the number of subpixels for each class according to the coarse fractions. To satisfy the constraints in (8), during the allocation process, each subpixel has to be assigned to only one class and the subpixels for each class have to be completely exhausted. A visiting path is then defined that determines the order of visited subpixels. Along this path, for a subpixel being visited, e.g., p_i, the K soft attribute values $Z_1(p_i), Z_2(p_i), \ldots, Z_K(p_i)$ are compared and ranked in a descending order. If the subpixels for the class with the highest soft attribute value, e.g., class k_0, have not been completely exhausted, then p_i is allocated to class k_0 (i.e., $x_{k_0}(p_i) = 1$, $x_{k \neq k_0}(p_i) = 0$); if the subpixels for k_0 have already been exhausted, p_i is allocated to the class whose subpixels have not been completely exhausted, as well as having the highest soft attribute value, and for the remaining subpixels, the soft attribute values for class k_0 are not considered in the comparisons any more.

UOS is a single-pass method, and thus, it involves no iteration [29]. The visiting order of subpixels in the UOS method is randomly determined. The visiting path has direct influence on the SPM performance, and different paths may result in different SPM results. There is much randomness, when the path is randomly determined, as there are $S^2!$ paths for each coarse pixel in all. The experimental results in the literature on UOS revealed that many speckle artifacts appear in the SPM results [31].

C. HAVF

Similar to UOS, another sequential-assignment-based class allocation method, i.e., HAVF, is also realized by direct comparison of soft attribute values. HAVF has been applied to BPNN [19], SPSAM [20], and ICK [32]. In each comparison, however, HAVF does not only compare K soft attribute values for a subpixel but also KS^2 values for all S^2 subpixels and K classes within a particular coarse pixel. The highest soft attribute value is found out, and the corresponding subpixel is also selected out meanwhile. The selected subpixel is allocated to its dominant class, on condition that the subpixels for this class have not been completely exhausted; otherwise, all S^2 soft attribute values for this class are set to a value less than 0 to be excluded in the following comparisons. When the selected subpixel is successfully allocated to a class, the K soft attribute values for this subpixel are also set to a value less than 0. The process is terminated when all S^2 subpixels within each coarse pixel are allocated.

HAVF is also noniterative and reproduces exactly the coarse fraction data. Different from UOS, for each coarse pixel, each subpixel in the visiting path in the HAVF method is found by comparison of all KS^2 values. Therefore, for each coarse pixel, the visiting path is unique, rather than a random one (as in UOS). Note that for UOS and HAVF, a normalization

procedure is suggested [9], [19], [20]. Specifically, within each coarse pixel, each soft attribute value is divided by the sum of S^2 attribute values from the same class. This adjustment is advantageous in cases where subpixels are surrounded by small fractions of a certain class and soft attribute values for this class are small [19], [20]. This normalization procedure is performed previous to that in (6).

IV. UOC

From LOT, UOS, and HAVF, we can learn that three tasks should be completed during the class allocation process for STHSPM algorithms.

1) For each subpixel, it should be assigned to one and only one class.
2) For each class, the number of subpixels belonging to it should be consistent with the coarse fraction data, and they should be completely exhausted during the class allocation process.
3) Attempt to maximize the objective function in (8).

Based on these three aspects, a new class allocation method, i.e., UOC, is proposed in this paper. In UOC, subpixels for each class are allocated in turn. Actually, UOS and HAVF start with 1) whereas the proposed UOC starts with 2).

A. Implementation of UOC

The implementation of UOC includes the following six steps.

Step 1: Define a visiting order of K classes, i.e., $k_1, k_2, \ldots, k_K$. This order can be defined randomly or by Moran's I (see Section IV-B for details).

Step 2: For the being visited class, e.g., k_r, the number of subpixels belonging to it in coarse pixel P_t is determined as $F_{k_r}(P_t)S^2$.

Step 3: At the current coarse pixel P_t, rank the S^2 soft attribute values $Z_{k_r}(p_1^t), Z_{k_r}(p_2^t), \ldots, Z_{k_r}(p_{S^2}^t)$ that have been obtained by any STHSPM algorithm in Section II, in a decreasing order, and a new sequence is generated, i.e., $Z_{k_r}(p_{D_1}^t), Z_{k_r}(p_{D_2}^t), \ldots, Z_{k_r}(p_{D_{S^2}}^t)$.

Step 4: According to aforementioned tasks 2) and 3) in Section IV, the first $NCr(NCr = F_{k_r}(P_t)S^2)$ subpixels in the new sequence, i.e., $p_{D_1}^t, p_{D_2}^t, \ldots, p_{D_{NCr}}^t$, are allocated to class k_r.

Step 5: According to task 1), the already allocated subpixels should not be considered in the allocation for remaining classes. To guarantee that, all soft attribute values for the next visited class k_{r+1} are adjusted by

$$Z_{k_{r+1}}\left(p_i^t\right) = Z_{k_{r+1}}\left(p_i^t\right) - c\sum_{j=1}^{r} x_{k_j}\left(p_i^t\right) \qquad (11)$$

where $c > 1$ is a coefficient. After adjustment, at any already allocated subpixel p_a,

$$\left.\begin{array}{l} \sum_{j=1}^{r} x_{k_j}(p_a) = 1 \\ Z_{k_{r+1}}(p_a) \in [0, 1] \end{array}\right\} \Rightarrow \left[Z_{k_{r+1}}(p_a) - c\sum_{j=1}^{r} x_{k_j}(p_a) \right]$$

$$\in [-c, 1-c] \quad (12)$$

which indicates with (11), the soft attribute values for the next visited class k_{r+1} at already allocated subpixels are automatically suppressed to be less than $0 (1 - c < 0)$ On the other hand, at any unallocated subpixel p_{ua},

$$\left.\begin{array}{l} \sum_{j=1}^{r} x_{k_j}(p_{ua}) = 0 \\ Z_{k_{r+1}}(p_{ua}) \in [0, 1] \end{array}\right\} \Rightarrow Z_{k_{r+1}}(p_{ua}) - c \sum_{j=1}^{r} x_{k_j}(p_{ua})$$
$$= Z_{k_{r+1}}(p_{ua}) \in [0, 1] \quad (13)$$

which indicates that the soft attribute values at unallocated subpixels do not make any change using adjustment in (11). From (12) and (13), it can be concluded that, after adjustment, the following equation holds:

$$Z_{k_{r+1}}(p_a) < Z_{k_{r+1}}(p_{ua}). \quad (14)$$

Since the number of subpixels for class k_{r+1} is less than the number of unallocated subpixels, adjustment in (11) ensures that the already allocated subpixels will not be allocated to class k_{r+1} any more. Therefore, the adjustment in (11) is an adaptive and simple scheme that does not need to artificially find out the already allocated subpixels or particularly exclude them during the class allocation process. Using (11), only one simple command is needed to exclude the already allocated subpixels for class allocation, as shown in the last sentence in the pseudocode given below. Note that c can take any value greater than 1 to ensure $1 - c < 0$, and it does not have any influence on the following class allocation process as it does not change the soft attribute values at unallocated subpixels at all.

Step 6: The whole process is terminated when all MS^2 subpixels are allocated.

Algorithm: Class allocation based on UOC

Inputs:
Soft attribute values $\{Z_k(p_i^t) | i = 1, \ldots, S^2; \ t = 1, \ldots, M; \ k = 1, \ldots, K\}$;
Class fractions $\{F_k(P_t) | t = 1, 2, \ldots, M; \ k = 1, 2, \ldots, K\}$ and zoom scale factor S.

Define a visiting order of K classes: $k_1, k_2, \ldots, k_K$
for $r = 1 : K$
    for $t = 1 : M$
        Rank sequence $Z_{k_r}(p_1^t), Z_{k_r}(p_2^t), \ldots, Z_{k_r}(p_{S^2}^t)$ in a decreasing order: $Z_{k_r}(p_{D_1}^t), Z_{k_r}(p_{D_2}^t), \ldots, Z_{k_r}(p_{D_{S^2}}^t)$
        for $i = 1 : F_{k_r}(P_t)S^2$
            $x_{k_r}(p_{D_i}^t) = 1$
        end
        for $i = F_{k_r}(P_t)S^2 + 1 : S^2$
            $x_{k_r}(p_{D_i}^t) = 0$
        end
    end
    Image $Z_{k_{r+1}}$ is updated by $Z_{k_{r+1}} = Z_{k_{r+1}} - c \sum_{j=1}^{r} x_{k_j}$
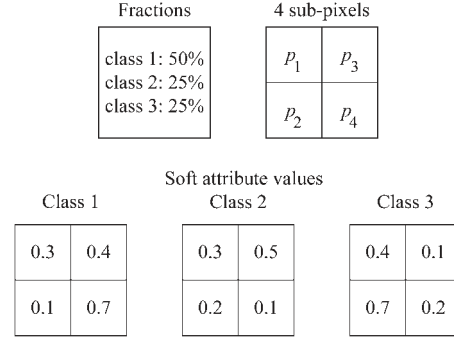end

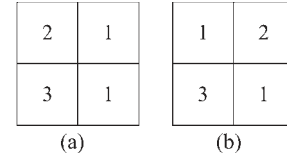Fig. 2. Illustration of the necessity of the adjustment in (11).

Fig. 3. Follow-up to Fig. 2. Two different SPM results generated along two different visiting orders of classes in UOC. (a) Class order: 1-2-3. (b) Class order: 2-1-3.
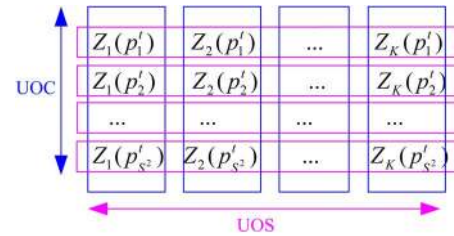

Fig. 4. Difference between UOC and UOS: comparisons in different units.

TABLE I
STATISTICS OF SOFT ATTRIBUTE VALUE COMPARISON DURING CLASS ALLOCATION PROCESS FOR UOS, HAVF, AND UOC (ANALYZED FOR A SINGLE COARSE PIXEL)

	Comparison times	Elements involved in each comparison
UOS	S^2	K
HAVF	$[S^2, K+S^2)$	KS^2
UOC	K	S^2

Outputs:
Binary class indicators $\{x_k(p_i^t) | i = 1 \ldots, S^2; \ t = 1, \ldots, M; \ k = 1, \ldots, K\}$

Without the adjustment in (11), some subpixels would be allocated to more than one class, and some subpixels would not be allocated to any class as a result. This conflicts with the aforementioned task 1). An example in Fig. 2 is used to illustrate the necessity of the adjustment in (11). Suppose a coarse pixel covers three land cover classes, i.e., classes 1, 2, and 3, and the fraction of the three classes are 50%, 25%, and 25%. With a zoom scale $S = 2$, there should be two, one, and one subpixels assigned to classes 1, 2, and 3, respectively. Let the visiting order of the three classes be 1-2-3. According to the soft attribute values of class 1, subpixels p_4 and p_3 are allocated to this class first. Without the adjustment, however,
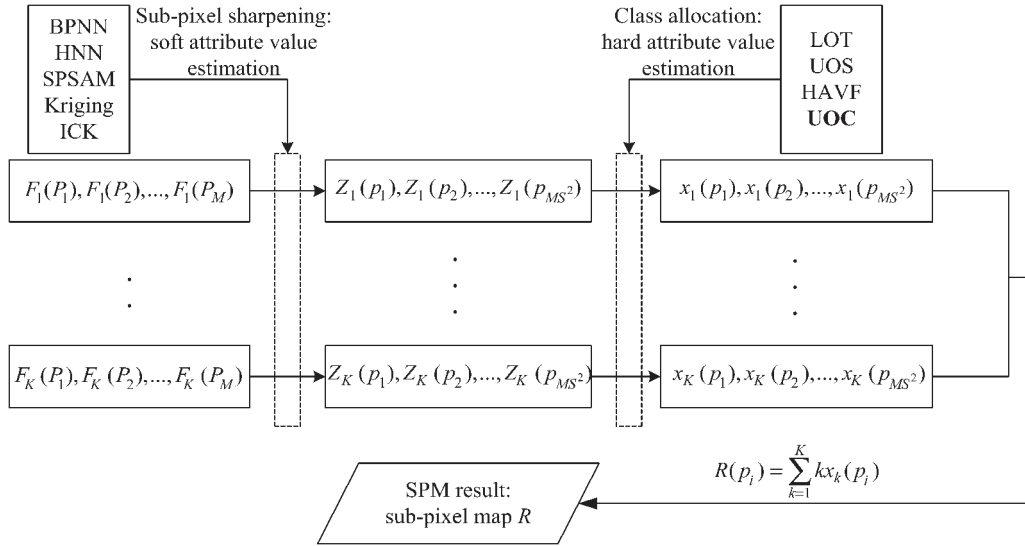
Fig. 5. Systemic framework of STHSPM algorithms, where the proposed class allocation method UOC is in bold.

when class 2 is visited, p_3 is again allocated to class 2, as 0.5 is the largest value among the four soft attribute values of class 2. Consequently, p_2 will be allocated to class 3, and p_1 will not be allocated to any class. If adjustment in (11) is applied (c is set to 2), when class 2 is visited after class 1, the four soft attribute values of class 2 are adjusted to $Z_2(p_1) = 0.3$, $Z_2(p_2) = 0.2$, $Z_2(p_3) = -1.5$, and $Z_2(p_4) = -1.9$. $Z_2(p_3)$ and $Z_2(p_4)$ are very small after adjustment, and p_4 and p_3 will not be considered in the allocation for class 2. Instead, p_1 will be allocated to class 2, and p_2 will be allocated to class 3 as a result.

B. Visiting Order of Classes Specified by Moran's I

In UOC, there are $K!$ visiting orders of classes in all, and different orders may lead to different SPM results. This can be also illustrated by the example in Fig. 2. Along two different visiting orders, such as 1-2-3 and 2-1-3, different SPM results are generated (see Fig. 3). The visiting order in UOC, therefore, should be specified reasonably.

Moran's I is an index of spatial autocorrelation for the landscape [14]. In [14], Moran's I was used to determine the order of input classes for pixel-swapping algorithm that was extended to multiple classes. Here, it is employed to determine a reasonable visiting order of classes in UOC. The index can be estimated from an available high spatial resolution land cover map. The map needs to be representative of the studied area for SPM. Moran's I for the kth class, i.e., I_k, is calculated as

$$I_k = \frac{V \sum_{i=1}^{V} \sum_{j=1}^{V} W_{ij} [x_k(p_i) - \overline{x_k}][x_k(p_j) - \overline{x_k}]}{\left(\sum_{i=1}^{V} \sum_{j=1}^{V} W_{ij}\right) \sum_{i=1}^{V} [x_k(p_i) - \overline{x_k}]^2} \quad (15)$$

where

$$W_{ij} = \begin{cases} 1, & \text{if } p_i \text{ and } p_j \text{ are neighbors} \\ 0, & \text{otherwise} \end{cases} \quad (16)$$

Fig. 6. Reference land cover map in the first experiment.

and V is the number of pixels in the high spatial resolution map. $\overline{x_k}$ is the mean of all binary class indicators for the kth class. In this paper, eight nearest neighbors are considered in (16).

If the high spatial resolution map is available, it can be readily used for Moran's I estimation. A critical issue, however, is that such high spatial resolution images are not obtainable in general. For this reason, a novel method to calculate Moran's I without high spatial resolution map is proposed, which estimates the index by directly using the fraction image of each class. Although the fraction images are in coarse spatial resolution, they contain spatial distribution characteristics for land cover classes. With the novel method, I_k is calculated as

$$I_k = \frac{M \sum_{i=1}^{M} \sum_{j=1}^{M} W_{ij} [F_k(P_i) - \overline{F_k}][F_k(P_j) - \overline{F_k}]}{\left(\sum_{i=1}^{M} \sum_{j=1}^{M} W_{ij}\right) \sum_{i=1}^{M} [F_k(P_i) - \overline{F_k}]^2} \quad (17)$$

where $\overline{F_k}$ is the mean of all fractions for the kth class in fraction image F_k. I_k take values in the range $[-1, 1]$, and -1
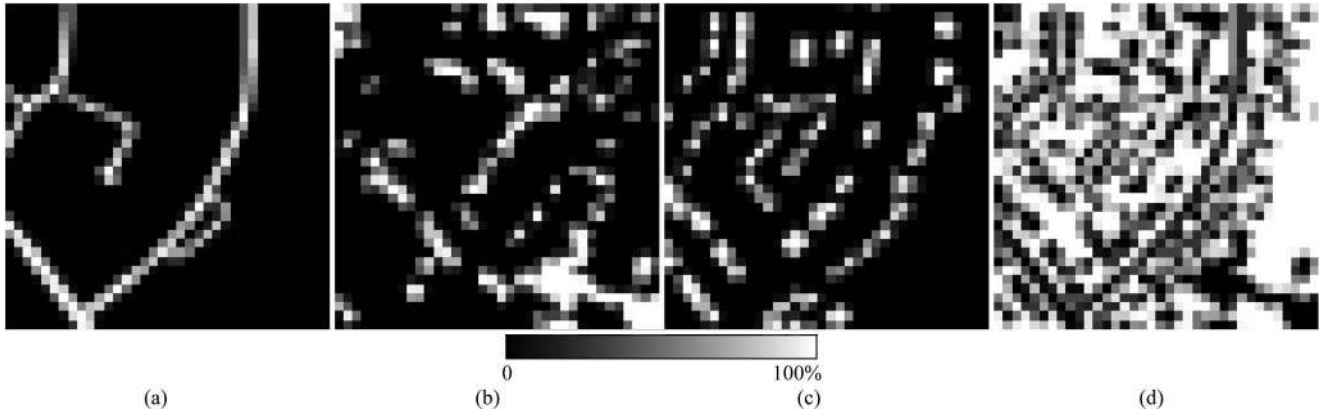
Fig. 7. Fraction images produced by degrading the reference land cover map in the first experiment with $S = 10$. (a) Roads. (b) Trees. (c) Buildings. (d) Grass.

and 1 indicate the weakest and the strongest autocorrelation, respectively. After the indexes of K classes are calculated, they are ranked in a decreasing order, and the classes with higher indexes are visited first.

C. Comparison With UOS, HAVF, and LOT

Similar to UOS and HAVF, UOC is also a sequential-assignment-based class allocation method. All of them are single-pass methods that are free of iteration and thus are fast. Moreover, all three methods are performed under the condition of reproducing exactly the coarse fractions. The core difference between UOS and UOC is that comparisons of soft attribute values are implemented in different units (see Fig. 4). More precisely, UOS compared K soft attribute values of K classes at the being visited subpixel, whereas UOC compared S^2 soft attribute values for the being visited class within each coarse pixel. UOS and UOC allocate classes for subpixels along paths, which determine the order of visited subpixels and classes.

Compared with LOT, a significant advantage of UOC is its less computing complexity. For each coarse pixel, LOT solves a linear problem involving KS^2 variables and $K + S^2$ equality constraints, as listed in (8). The optimal solution is obtained after numbers of iterations. When K or S, or even M, is large, the whole process will be considerably CPU demanding. As for UOC, for each coarse pixel, only K comparisons need to be carried out, and the output of each comparison is a sequence, which is used to select out the subpixels for the corresponding class, as shown in Step 3 in Section IV-A. The comparisons in UOC require less time, far less than LOT does.

Table I summarizes the soft attribute value comparison for three sequential-assignment-based class allocation methods, i.e., UOS, HAVF, and UOC. As shown in the table, for each coarse pixel, UOS and UOC need S^2 and K comparisons, and K and S^2 elements are involved in each comparison for the two methods; HAVF sometimes need more than S^2 comparisons, because the subpixels for the class, to which the highest soft attribute value corresponds, may have been exhausted and the selected subpixel will not be allocated to any class for that comparison. For HAVF, KS^2 elements are compared each time. Obviously, HAVF requires more time than UOS to complete class allocation. Similar to UOC, the consuming time of UOS and HAVF is generally less than that of LOT, since the value comparison is easy and fast for computers to realize.

TABLE II
MORAN'S I OF FOUR CLASSES AT DIFFERENT SCALES
IN THE FIRST EXPERIMENT

	$S=1$	$S=5$	$S=10$
Roads	0.9243	0.7227	0.5034
Trees	0.9130	0.7123	0.4919
Buildings	0.8961	0.6577	0.3590
Grass	0.8731	0.5715	0.2850
Specified order	Roads-Trees -Buildings-Grass	Roads-Trees -Buildings-Grass	Roads-Trees -Buildings-Grass

UOC is processed on K soft-classified images at fine spatial resolution one by one. Each soft-classified image encapsulates spatial continuity for the corresponding class. That is, within each coarse pixel, subpixels with large soft attribute values for the same class tend to stay together. Using UOC, subpixels staying together are more likely to be allocated to the same class than distant subpixels. In this way, autocorrelation for each class can be maximized by Step 4 in Section IV-A, which is not the case in LOT, UOS, and HAVF. According to spatial dependence principle that underpins SPM, the intraclass spatial correlation is expected to be maximized, which can just been done by UOC. For UOC, this is the unique advantage over LOT, UOS, and HAVF when it is applied to STHSPM algorithms.

After description of five STHSPM algorithms, existing LOT, UOS, HAVF, and the proposed UOC, the systemic framework of STHSPM algorithms are shown in Fig. 5.

V. EXPERIMENTS AND ANALYSIS

A. Experimental Setup and Accuracy Assessment

To demonstrate the effectiveness and advantages of the proposed UOC-based class allocation method for STHSPM algorithms, experiments on three remote sensing images were implemented. UOC was applied to all the five STHSPM algorithms introduced in Section II, i.e., BPNN, HNN, SPSAM, kriging, and ICK. UOC was also compared with LOT-, UOS-, and HAVF-based class allocation methods. All experiments were tested on an Intel Core 2 Processor (1.800-GHz Duo central processing unit, 2.00-GB random access memory) with MATLAB 7.1 version. For BPNN, a 3×3 local window was
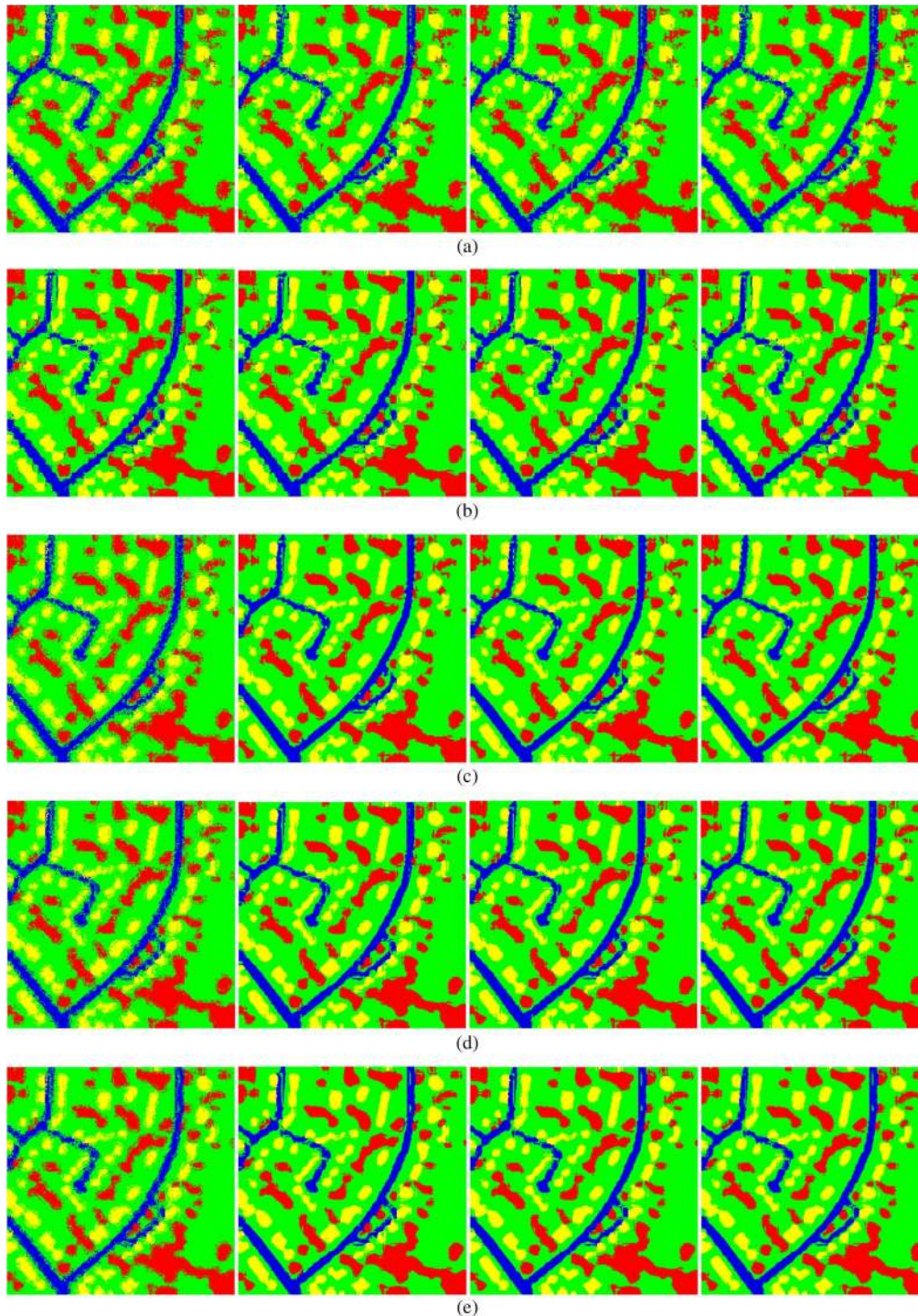
Fig. 8.   SPM results of five STHSPM algorithms combined with UOS-, HAVF-, LOT-, and UOC-based class allocation methods in the first experiment ($S = 10$). (a) BPNN. (b) HNN. (c) SPSAM. (d) Kriging. (e) ICK. From left to right: UOS (a random realization), HAVF, LOT, and UOC (visiting order specified by Moran's I).

used to extract the inputs of both training and test samples, and the parameters involved in this method were set to the same values as in [22]. The parameters in HNN were the same as in [49].

To objectively evaluate and solely concentrate on the performance of the proposed UOC, in the first and second experiments, the studied coarse images were produced by degrading hard-classified reference land cover maps using an $S \times S$ mean filter. The synthetic coarse images were considered as outputs

of soft classification. SPM algorithms were processed on the coarse images to yield land cover maps having the same spatial resolution as the corresponding reference maps, by zooming in the coarse images with the scale factor S. The advantages of using such synthetic coarse images include: 1) errors from soft classification and some other processes (e.g., registration) are avoided [50], and the test is directed at the SPM algorithm itself [46]; 2) the reference land cover maps are completely reliable for accuracy assessment. In the third experiment, a
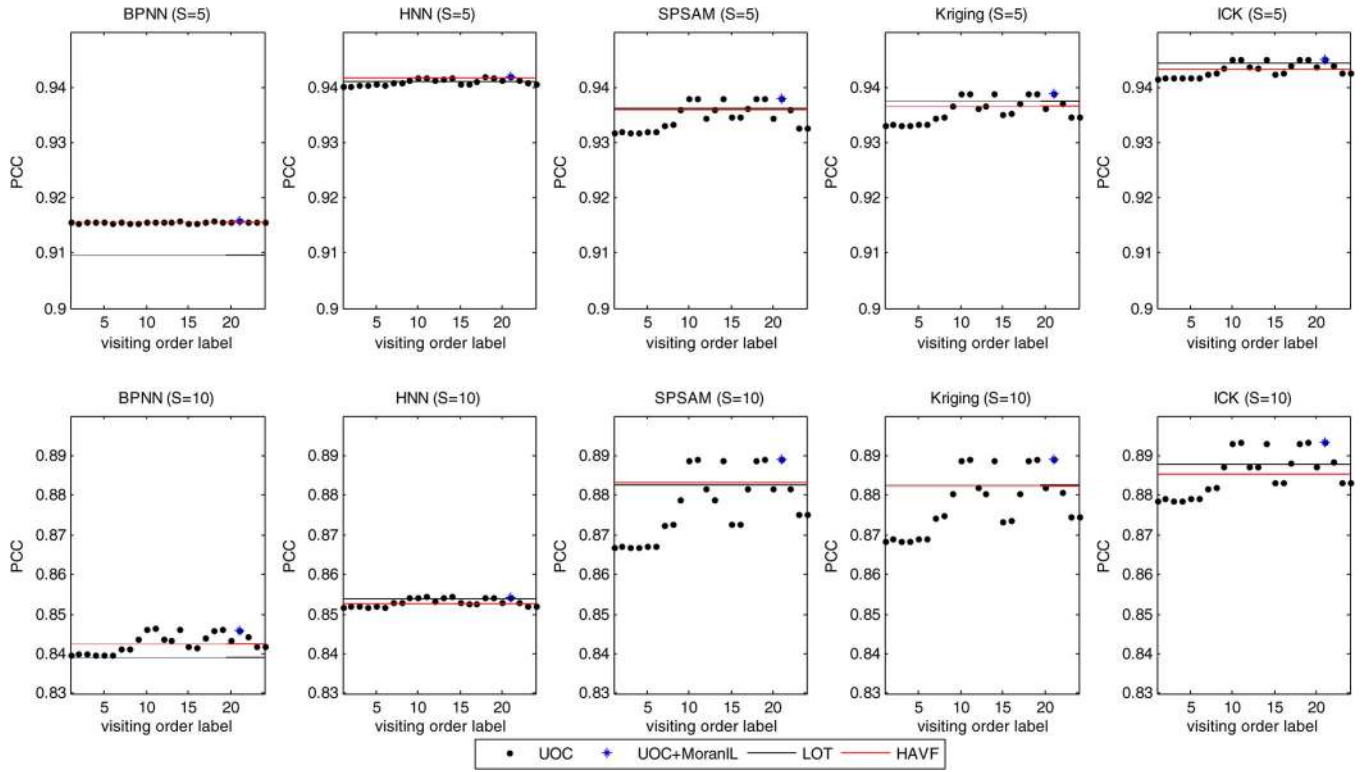
Fig. 9. PCC of five STHSPM algorithms combined with HAVF, LOT, and UOC at $S = 5$ and 10 in the first experiment. UOC+MoranIL means UOC with Moran's I estimated from low spatial resolution fraction images.

coarse image was produced by degrading a Landsat TM image. Soft classification was then implemented on the coarse image to generate fractions, with SPM subsequent to that. By such a setup, inherent uncertainty in soft classification was taken into consideration [46], and the fractions are more similar to those in real applications, in comparison with those in the first two experiments.

SPM is essentially a hard classification technique carried out at the subpixel level. The accuracy of hard classification algorithms is usually evaluated quantitatively by the overall accuracy, in terms of the percentage of correctly classified pixels (PCC). Due to that, PCC was used for accuracy assessment on SPM results in all three experiments. To evaluate the statistical significance in accuracy for different STHSPM algorithms and class allocation methods, McNemar's test [51] was also applied. The significance of the difference between two classification results is determined by

$$z_{01} = \frac{f_{01} - f_{10}}{\sqrt{f_{01} + f_{10}}} \tag{18}$$

where f_{01} are the number of pixels that are correctly classified in result 0 but incorrectly classified in result 1 and f_{10} vice versa. Using the 95% degree of confidence level, the difference between two classification results is considered to be statistically significant if $|z_{01}| > 1.96$.

B. Experiment 1

In the first experiment, a land cover map of an area in Bath, U.K., was studied, as shown in Fig. 6 (provided by Dr. A. J. Tatem). The land cover map was obtained by manual

TABLE III
PCC (%) OF UOS METHOD IN EXPERIMENT 1 (AVERAGES OF 100 RUNS ± STANDARD DEVIATION)

	S=5	S=10
BPNN	87.77±0.09	81.36±0.06
HNN	90.35±0.06	83.21±0.04
SPSAM	81.64±0.12	79.61±0.09
Kriging	83.00±0.14	80.33±0.07
ICK	83.72±0.11	80.84±0.06

TABLE IV
LABELS OF 24 VISITING ORDERS IN UOC (C1, C2, C3, AND C4 DENOTE ROADS, TREES, BUILDINGS, AND GRASS)

1	C4-C3-C2-C1	2	C4-C3-C1-C2	3	C4-C2-C3-C1
4	C4-C2-C1-C3	5	C4-C1-C2-C3	6	C4-C1-C3-C2
7	C3-C4-C2-C1	8	C3-C4-C1-C2	9	C3-C2-C4-C1
10	C3-C2-C1-C4	11	C3-C1-C2-C4	12	C3-C1-C4-C2
13	C2-C3-C4-C1	14	C2-C3-C1-C4	15	C2-C4-C3-C1
16	C2-C4-C1-C3	17	C2-C1-C4-C3	18	C2-C1-C3-C4
19	C1-C3-C2-C4	20	C1-C3-C4-C2	21	C1-C2-C3-C4
22	C1-C2-C4-C3	23	C1-C4-C2-C3	24	C1-C4-C3-C2

digitizing of the aerial photograph in [52]. The map contains 360×360 pixels and covers four classes, namely, roads, trees, buildings, and grass. The roads and buildings mainly appear as straight lines and right angles, respectively. The spatial

TABLE V
MCNEMAR'S TEST FOR DIFFERENT CLASS ALLOCATION METHODS IN THE FIRST EXPERIMENT (0: UOC+MORANIL; 1: UOS; 2: HAVF; 3: LOT)

	S=5			S=10		
	z_{01}	z_{02}	z_{03}	z_{01}	z_{02}	z_{03}
BPNN	[27.0416, 29.7322]	0.8752	8.4650	[27.6674, 29.8159]	10.6104	11.0707
HNN	[31.3720, 33.4408]	0.6266	3.7311	[24.1120, 26.2680]	3.4411	1.7018
SPSAM	[63.2862, 65.9140]	8.0641	7.2449	[66.6251, 69.4362]	16.4369	16.4028
Kriging	[59.4212, 62.0354]	8.7551	7.2638	[62.9627, 64.9855]	18.0859	17.2707
ICK	[59.8257, 62.3790]	7.8893	4.3911	[63.2382, 65.4879]	21.0428	16.8453

pattern of trees is more complex and irregular. The map was degraded with two scales, i.e., $S = 5$ and 10, to generate two coarse images. The fraction images of four classes in the coarse image generated with $S = 10$ are shown in Fig. 7. From these fraction images, it can be seen clearly that the coarse proportion information is insufficient to represent the spatial distribution of land cover classes, which indicates the necessity of SPM in land cover information extraction.

The five STHSPM algorithms, i.e., BPNN, HNN, SPSAM, kriging, and ICK, were then processed on the two coarse images generated with $S = 5$ and 10 to reconstruct the land cover maps having the same spatial resolution as that in Fig. 6. The reference map in Fig. 6 was used to extract training samples for BPNN and indicator semivariograms for ICK. Table II lists Moran's I of the four classes in different spatial resolution images and the corresponding specified visiting orders of four classes. Here, $S = 1$ means the indexes were calculated using (15), which is based on the assumption that the required high spatial resolution map (i.e., Fig. 6) is available. For two coarse images, the indexes of classes were calculated using our proposed method in (17). As shown in the table, in this experiment, the orders specified by two approaches at three scales are the same.

Fig. 8 shows the SPM results for the coarse fraction images in Fig. 7. The five STHSPM algorithms were combined with UOS-, HAVF-, LOT-, and UOC-based class allocation methods. The results of UOC shown in Fig. 8 were produced with a specified order at $S = 10$ (i.e., roads-trees-buildings-grass), as listed in Table II. For UOS, the results generated with a random visiting order of subpixels for five STHSPM algorithms are shown in the first column in Fig. 8. As can be seen from the maps, there are many speckle artifacts in SPM results while using UOS for class allocation. In comparison with UOS, much less speckle artifacts are generated by HAVF and LOT, and both of them can obviously obtain better results than UOS. Focusing on maps yielded by the proposed UOC, the boundaries of classes are clearer than those in UOS, HAVF, and LOT results. There are fewer isolated pixels in UOC results, which is particularly well illustrated by the restoration of roads in five maps in the last column. Among the four class allocation methods, UOC produces the most satisfactory fine spatial resolution maps.

The SPM results were also assessed quantitatively by PCC. As can be observed in the fraction images in Fig. 7, there are some pure coarse pixels containing only one land cover class. In SPM, all subpixels within the pure pixel are allocated to the same class to which the pure pixel belongs. This simple copy process only raises PCC without providing useful information about the SPM algorithms' prediction abilities [7], [8], [12],

TABLE VI
RUNNING TIME (IN SECONDS) OF EACH CLASS ALLOCATION
METHOD IN THE FIRST EXPERIMENT

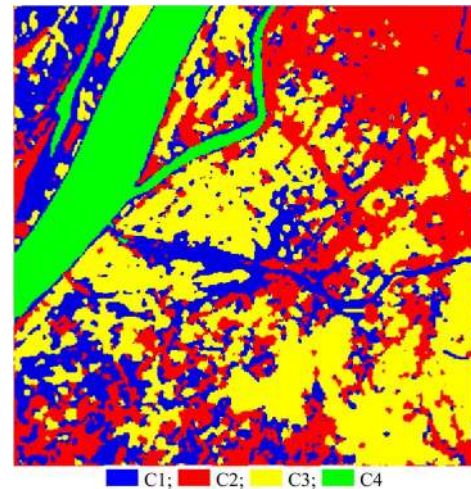|	LOT	UOS	HAVF	UOC
S=5	135	2	3	2
S=10	380	4	7	2

Fig. 10. Reference land cover map in the second experiment.

[53], [54]. To eliminate the influence brought by the pure pixels, subpixels within them were excluded in the accuracy statistics in this experiment. Fig. 9 shows the PCC of five STHSPM algorithms combined with HAVF, LOT, and UOC, at $S = 5$ and 10, corresponding to ten subfigures in all. To clearly exhibit the differences between the lines of LOT and HAVF, the PCC of UOS is not shown in Fig. 9, but in Table III instead. Because different visiting paths of subpixels lead to different SPM results in UOS, 100 random paths were tested for UOS. In all ten cases, the PCC of UOS is lower than that of HAVF, LOT, and UOC. The PCC of UOC with all 24 (4! = 24) visiting orders are also displayed in Fig. 9. The labels for the corresponding visiting orders are illustrated in Table IV. As shown in Table II, Moran's I estimated from both high and low spatial resolution images specify the same visiting order of classes in UOC in this experiment. Therefore, we only consider the UOC+MoranIL case, which means UOC with specified order by Moran's I estimated from low spatial resolution fraction images.

Comparing PCC at different scale factors, we can clearly see that as the scale factor increases, the accuracies of SPM
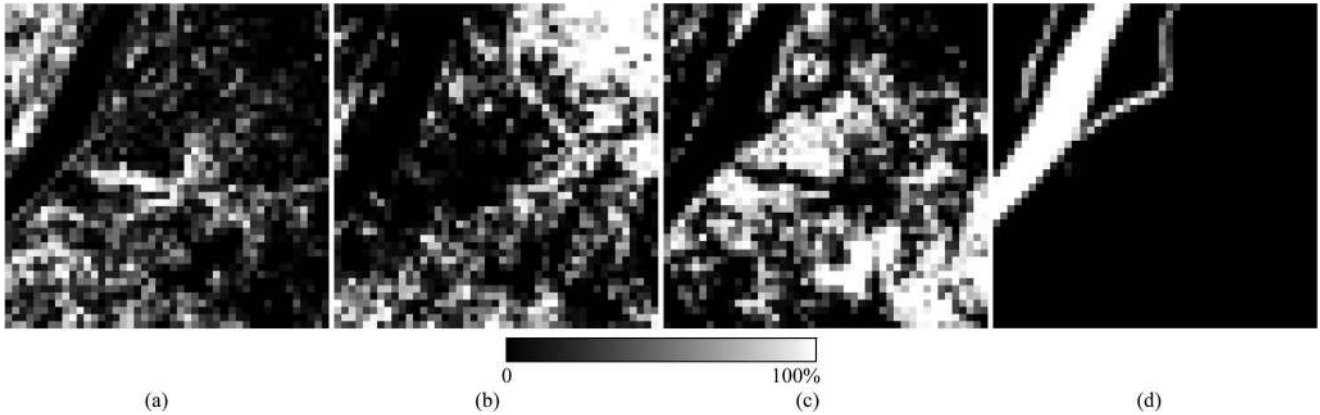
Fig. 11. Fraction images of the four classes produced by degrading the reference land cover map in the second experiment with $S = 8$. (a) C1. (b) C2. (c) C3. (d) C4.

decrease (see Fig. 9). The reason is that the SPM problem becomes more complicated with higher scale factors, as for each coarse pixel, the spatial locations of more subpixels need to be estimated and uncertainty increases [8], [19]. More precisely, at $S = 5$ and 10, the locations of 25 and 100 subpixels need to be predicted within each coarse pixel. While observing the data for UOC in each subfigure, it can be found that different visiting orders of classes result in different SPM accuracies, which is particularly obvious in SPSAM, kriging, and ICK results. Hence, the visiting order in UOC has direct influence on SPM accuracy. When Moran's I is applied in UOC (i.e., UOC+MoranIL) in each STHSPM algorithm, the highest accuracy is achieved among all 24 orders, which indicates that Moran's I is able to select out the best visiting order in UOC and also validates the effectiveness of using Moran's I gained from coarse fraction images in UOC. Furthermore, from the comparison of the PCC of UOC+MoranIL, HAVF, and LOT, we can conclude that UOC+MoranIL is capable of producing higher accuracy than HAVF and LOT in all cases.

Table V lists the McNemar's test results for UOS, HAVF, LOT, and UOC+MoranIL that were applied to five STHSPM algorithms. The statistically insignificant values at the 95% confidence level are underlined. As can be concluded from these values, UOC+MoranIL produces significantly higher accuracy than the other three class allocation methods in nearly all cases. This reveals that the intraclass spatial correlation is more important than the objective function in (8) in this experiment. With a reasonably specified visiting order of classes, UOC maximized the spatial autocorrelation of each class, which was not well taken into consideration in UOS, HAVF, and LOT.

In addition, the running time of the four class allocation methods in this experiment is given in Table VI. Note that, for each method, the hard class labels of subpixels within pure coarse pixels were determined by the simple copy process. The consuming time of three soft attribute comparison-based methods, i.e., UOS, HAVF, and UOC, has the same order of magnitudes, which is less than 10 s and much less than that of LOT. More precisely, LOT needs several minutes to complete the class allocation process at both scales. The running time of LOT increases from 135 to 380 s when S increases from 5 to 10, because at $S = 5$, the optimization problem in LOT contains 100 variables and 29 equality constraints at each coarse pixel, whereas at $S = 10$, the corresponding number of variables and equality constraints increase to 400 and 104,

TABLE VII
MORAN'S I OF FOUR CLASSES AT DIFFERENT
SCALES IN THE SECOND EXPERIMENT

	S=1	S=8	S=12
C1	0.7355	0.5505	0.5406
C2	0.8229	0.6558	0.6628
C3	0.8410	0.6224	0.5914
C4	0.9622	0.8470	0.8038
Specified order	C4-C3	C4-C2	C4-C2
	-C2-C1	-C3-C1	-C3-C1

respectively. However, for UOS, HAVF, and UOC, within 10 s were consumed because only comparisons of soft attribute values were carried out and no complex processes are involved.

C. Experiment 2

A land cover map of an area in Nanjing, China, was used for test in the second experiment (see Fig. 10). This map was derived from a 30-m spatial resolution image in [55], using a maximum-likelihood classifier (MLC) along with a modal filter removing the noises in MLC results. The studied area contains 360×360 pixels and was assigned to four classes, namely, C1, C2, C3, and C4. Comparing Fig. 10 with Fig. 6, one can find that the distribution of the classes in this experiment is more random and more complex than that in the first experiment. The reference land cover map was degraded with $S = 8$ and 12, producing two different coarse spatial resolution images. Fig. 11 displays the fraction images of four land cover classes for $S = 8$. Table VII lists Moran's I of the four classes in different spatial resolution images and the corresponding specified visiting orders of four classes. Comparing the values at $S = 1$ in Table VII to those at $S = 1$ in Table II, we can find that the indexes of the four classes in this experiment are generally lower than those in the first experiment, as the spatial continuity of classes in Fig. 10 is weaker than that in Fig. 6. In addition, specified orders using Moran's I estimated from high spatial resolution map and low spatial resolution fraction images are different in this experiment.

The 20 SPM results for coarse fraction images in Fig. 11 are shown in Fig. 12, which were produced by combining the five STHSPM algorithms with UOS, HAVF, LOT, and UOC.
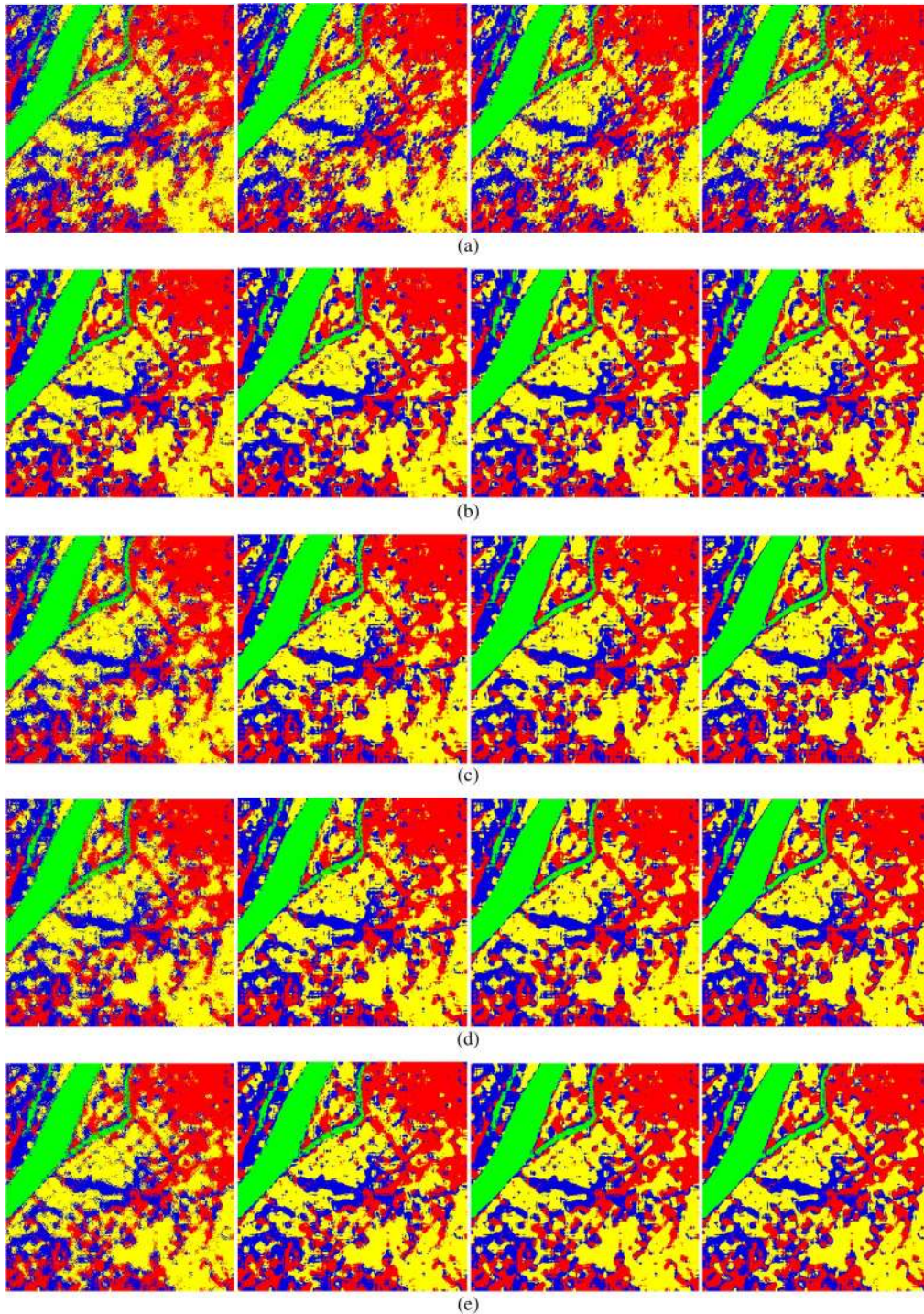
Fig. 12. SPM results of five STHSPM algorithms combined with UOS-, HAVF-, LOT-, and UOC-based class allocation methods in the second experiment ($S = 8$). (a) BPNN. (b) HNN. (c) SPSAM. (d) Kriging. (e) ICK. From left to right: UOS (a random realization), HAVF, LOT, and UOC (visiting order specified by Moran's I that was estimated from fraction images at $S = 8$).

For UOC, the visiting order of classes used was determined by Moran's I at $S = 8$. Again, many speckle artifacts appear in UOS results. HAVF obtains subpixel maps with much fewer speckle artifacts than UOS. However, the performance of HAVF is still poorer than that of LOT and UOC. For example, the boundaries of C4 in five HAVF results are rougher than those in LOT and UOC results. SPM results obtained with LOT and UOC look nearly the same, and both of them produce more satisfactory SPM results than UOS and HAVF.

In this experiment, subpixels within pure pixels were also excluded in quantitative assessment. The PCC of five STHSPM algorithms combined with four class allocation methods at $S = 8$ and 12 is shown in Fig. 13. In each subfigure, the PCC of UOS is the average of 100 runs. As for UOC, all 24 visiting orders of classes in UOC were tested, and labels for visiting orders are similar to those in Table IV. UOC+MoranIH and UOC+MoranIL mean that the visiting orders of classes in UOC were specified by Moran's I estimated from high spatial
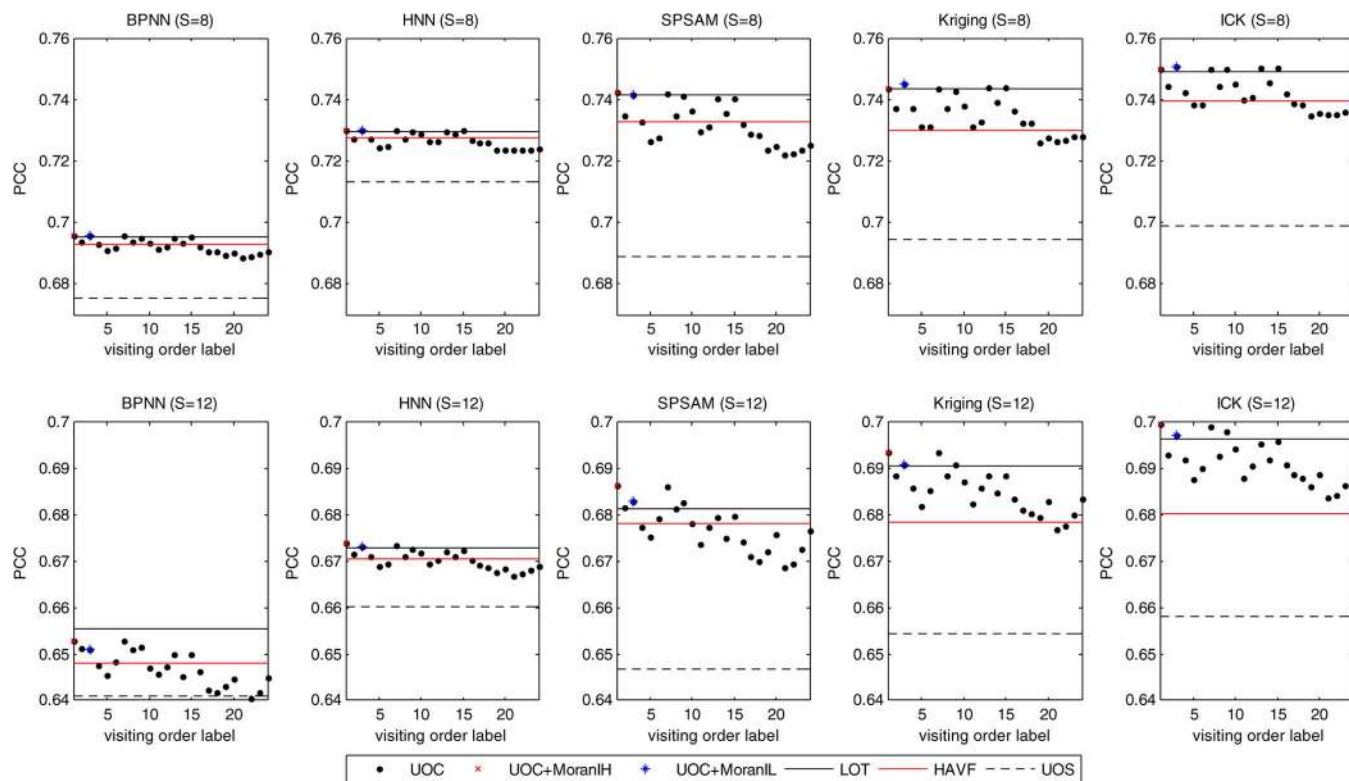
Fig. 13. PCC of five STHSPM algorithms combined with UOS, HAVF, LOT, and UOC at $S = 8$ and 12 in the second experiment. The PCC of UOS is the average of 100 runs; UOC+MoranIH and UOC+MoranIL mean UOC with Moran's I estimated from high spatial resolution map and low spatial resolution fraction images, respectively.

TABLE VIII
MCNEMAR'S TEST FOR DIFFERENT CLASS ALLOCATION METHODS IN THE SECOND EXPERIMENT (0: UOC+MORANIL; 1: UOS; 2: HAVF; 3: LOT)

	S=8			S=12		
	z_{01}	z_{02}	z_{03}	z_{01}	z_{02}	z_{03}
BPNN	[13.1000, 15.9465]	4.0308	*0.8109*	[5.7561, 8.8621]	2.7497	-4.0589
HNN	[14.7358, 17.4458]	3.4283	*1.2672*	[10.7939, 13.6949]	3.5008	*0.5605*
SPSAM	[35.3203, 37.7278]	9.7576	*0.0781*	[25.3217, 27.4400]	5.2029	1.9778
Kriging	[34.1852, 37.0153]	16.4837	2.1078	[26.0298, 28.6448]	12.8207	*0.7635*
ICK	[35.2192, 37.9695]	21.1905	*1.9010*	[27.8429, 30.7404]	16.9686	*1.2814*

resolution map and low spatial resolution fraction images, respectively.

As can be seen from the data in all ten subfigures, the performances of HAVF and LOT in five STHSPM algorithms are obviously superior to UOS. Compared with HAVF, LOT obtains higher accuracy. From the comparison between UOC and LOT, it is found that, when Moran's I is used in UOC, including both UOC+MoranIH and UOC+MoranIL, UOC is capable of producing slightly higher accuracy than LOT in nearly all cases. In addition, the accuracies of UOC+MoranIL are generally slightly lower than those of UOC+MoranIH. For BPNN at $S = 12$, the accuracies of both UOC+MoranIH and UOC+MoranIL are lower than those of LOT. This is because the output of the first step (i.e., subpixel sharpening result) in BPNN is not as accurate as those in the other four STHSPM algorithms, due to the inherent error in the BPNN model itself. In this case, the spatial continuity of each class encapsulated in the subpixel sharpening result of BPNN is not strong, and thus,

the performances of UOC+MoranIH and UOC+MoranIL are slightly poorer than LOT.

The McNemar's test results for UOS, HAVF, LOT, and UOC+MoranIL in five STHSPM algorithms are displayed in Table VIII. Likewise, 100 random paths for UOS were tested, and the statistically insignificant values at the 95% confidence level are underlined. In this experiment, UOC+MoranIL obtains significantly higher accuracy than UOS and HAVF for all five STHSPM algorithms. However, the PCC of UOC+MoranIL is insignificantly higher than that of LOT in most cases. This is because the intraclass spatial correlation in the studied area in this experiment is not very strong, as can be seen from Moran's I at $S = 1$ in Table VII, and thus, in terms of SPM accuracy, the advantage of UOC+MoranIL over LOT is not obvious.

However, UOC has significant advantage over LOT in terms of computing complexity. As shown in Table IX, at $S = 8$ and 12, LOT needs 360 and 700 s to complete class allocation

TABLE IX
RUNNING TIME (IN SECONDS) OF EACH CLASS ALLOCATION
METHOD IN THE SECOND EXPERIMENT

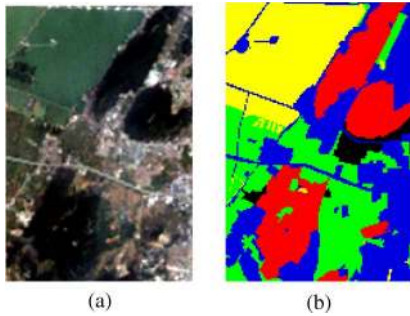|	LOT	UOS	HAVF	UOC
S=8	360	4	7	2
S=12	700	5	10	2

Fig. 14. Landsat TM image in experiment 3. (a) Color image (bands 3, 2, and 1 as RGB). (b) Reference land cover map: (blue) building, (red) woodland, (yellow) water, (green) farmland, (black) unclassified.

for each STHSPM algorithm. For the proposed UOC, it only consumes 2 s, much less than LOT does. Additionally, UOS and HAVF also need less time for the class allocation process.

D. Experiment 3

In the third experiment, a 30-m spatial resolution multispectral Landsat TM image (180 × 120 pixels) located in Xuzhou City, China, was used for test. The Landsat TM image was acquired in September 2000 and mainly covers four classes, namely, building, woodland, water, and farmland. Bands 1, 2, 3, 4, 5, and 7 were used in this experiment. The image and its reference land cover map are shown in Fig. 14. The reference land cover map in Fig. 14(b) was obtained with the aid of a 1:2000 land use map that was produced around the same date as the Landsat TM image. To consider the inherent uncertainty in soft classification and simulate SPM in real cases, the coarse image for SPM was generated by degrading the Landsat TM image with $S = 6$, and Fig. 14(b) can be then used for supervised accuracy assessment.

First, soft classification was implemented on the coarse image to generate fractions. Linear spectral mixture analysis (LSMA) [56] is widely used, appreciating its simple physical meaning and its convenience in application [49]. Here, LSMA was used for soft classification. The fraction images of four land cover classes are displayed in Fig. 15. SPM was then carried out to obtain a land cover map that has the same spatial resolution as that in Fig. 15. Moran's I of the four classes obtained with high spatial resolution map in Fig. 14(b) and fraction images in Fig. 15 are listed in Table X. As shown in the table, in this experiment, the specified order by the two approaches are the same. Since the effectiveness of using Moran's I in UOC has been demonstrated in the first and second experiments, in this experiment, only the visiting order of class specified by Moran's I was used for test of the UOC method.

The SPM results of five STHSPM algorithms combined with UOS, HAVF, LOT, and UOC are shown in Fig. 16. Due to the errors from soft classification, some pixels are unavoidably misclassified in the results. For instance, in all 20 maps, some
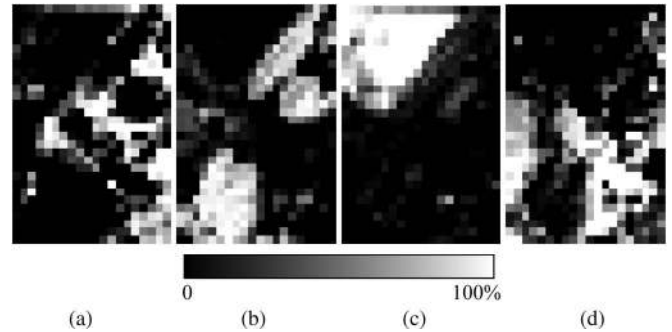

Fig. 15. Fraction images of the four classes in the degraded Landsat TM image. (a) Building. (b) Woodland. (c) Water. (d) Farmland.

pixels are misclassified as water class within the area of woodland class, which conflicts with the distribution of woodland in the reference map in Fig. 14(b). Errors from soft classification adversely affect the overall performance of SPM. Similar to the corresponding results in the first and second experiments, speckle artifacts were produced when UOS was applied for class allocation. From visual inspection, the results of HAVF, LOT, and UOC are close to each other, and all of them are evidently superior to UOS results.

Table XI lists the PCC of five STHSPM algorithms combined with UOS, HAVF, LOT, and UOC. In this experiment, PCC was calculated taking account of all 180 × 120 pixels (except the unclassified ones in Fig. 14) in each SPM result. The pure pixels in fraction images were not excluded in the accuracy statistics, as whether a pixel is pure or not is determined by the soft classifier LSMA. We also consider the performance of the soft classifier when a multispectral coarse image is studied for SPM [57]. This is different from the first and second experiments, where synthetic fraction images were studied and no soft classifier was applied in fact. UOS was also tested using 100 random paths. As can be concluded from the data in Table XI, the accuracies of HAVF, LOT, and UOC for each STHSPM algorithm are higher than those of UOS.

In Table XII, the McNemar's test results for four class allocation methods in five STHSPM algorithms are displayed. In 100 random realizations of UOS, PCC values of SPSAM, kriging, and ICK are all significantly lower than those of UOC; for BPNN and HNN, 78% and 63% of the PCC values are significantly lower than those of UOC. Focusing on values in the last two columns in Table XII, it can be concluded that the advantage of UOC over HAVF is obvious than that over LOT. In particular, in comparison with HAVF, when UOC is applied to ICK, UOC achieves significantly higher accuracy. For all five STHSPM algorithms, however, the differences between UOC and LOT in accuracy are statistically insignificant. The main reason is that errors from soft classification were propagated to SPM results [58] and suppressed the performances of UOC. In this experiment, UOC is considered to produce comparable SPM accuracy to LOT.

The running time of LOT, UOS, HAVF, and UOC in this experiment is 40, 2, 3, and 1 s, respectively. Again, UOC spends much less time than LOT. Through this experiment, the effectiveness and advantages of the proposed UOC are further demonstrated.

E. Intercomparison of Five STHSPM Algorithms

It is worth doing intercomparison of SPM algorithms, as expected in [46]. Here, the five STHSPM algorithms are
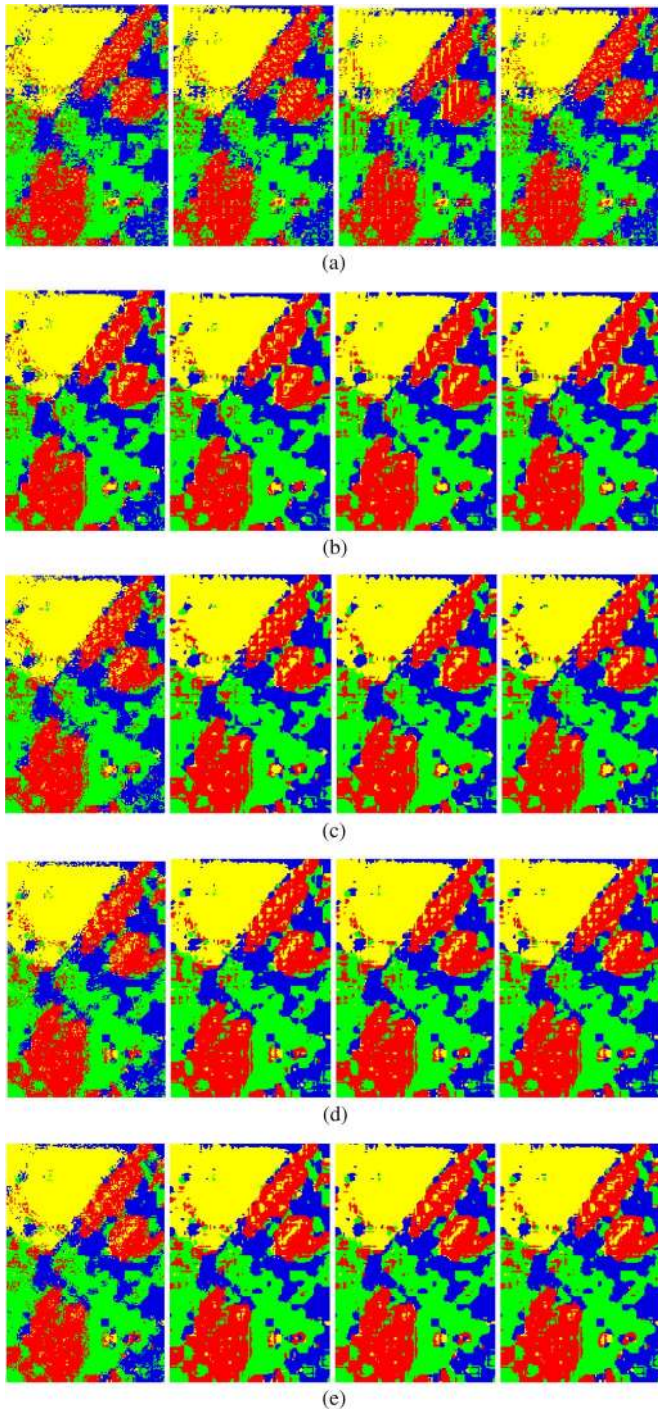
Fig. 16. SPM results of five STHSPM algorithms combined with UOS-, HAVF-, LOT-, and UOC-based class allocation methods in the third experiment ($S = 6$). (a) BPNN. (b) HNN. (c) SPSAM. (d) Kriging. (e) ICK. From left to right: UOS (a random realization), HAVF, LOT, and UOC (visiting order specified by Moran's I).

TABLE X
MORAN'S I OF FOUR CLASSES AT DIFFERENT SCALES IN THIRD SECOND EXPERIMENT

	S=1	S=6
Building	0.8318	0.5094
Woodland	0.9224	0.7353
Water	0.9369	0.8951
Farmland	0.8431	0.6153
Specified order	Water-Woodland -Farmland-Building	Water-Woodland -Farmland-Building

TABLE XI
PCC (%) OF FOUR CLASS ALLOCATION METHODS FOR FIVE STHSPM ALGORITHMS (THE DATA FOR UOS ARE AVERAGES OF 100 RUNS ± STANDARD DEVIATION AND THE VISITING ORDER OF CLASS SPECIFIED BY MORAN'S I WAS USED FOR UOC)

	UOS	HAVF	LOT	UOC
BPNN	70.54±0.09	71.11	71.23	71.08
HNN	71.01±0.06	71.25	71.43	71.38
SPSAM	70.08±0.07	71.09	71.27	71.24
Kriging	70.22±0.08	71.16	71.28	71.34
ICK	70.26±0.09	71.22	71.39	71.49

TABLE XII
MCNEMAR'S TEST FOR DIFFERENT CLASS ALLOCATION METHODS IN THE THIRD EXPERIMENT (0: UOC; 1: UOS; 2: HAVF; 3: LOT)

	z_{01}	z_{02}	z_{03}
BPNN	[1.1173, 3.3433]	-0.2739	-0.9261
HNN	[1.2835, 3.2513]	0.9365	-0.7581
SPSAM	[4.0758, 6.1144]	1.4888	-0.2466
Kriging	[3.9939, 5.5421]	1.6537	0.7278
ICK	[4.3572, 6.3084]	2.4283	1.0721

ICK is able to generate the best results among five STHSPM algorithms. Specifically, there are evident jagged boundaries in BPNN results. As for HNN, the distribution of classes looks more reasonable than that in BPNN results. However, the boundary of C4 is relatively rough when compared to ICK. Observing SPSAM results, we can find some cone-shaped objects in the map, particularly for those belonging to C2. Kriging provides more satisfactory results than BPNN, HNN, and SPSAM, but there are some linear artifacts. Compared with kriging results, in the map yielded by ICK, there are less linear artifacts, and the continuity of each class is stronger.

The quantitative comparison of five STHSPM algorithms is studied for the first and second experiments. The McNemar's test results for five STHSPM algorithms in the two experiments are shown in Tables XIII and XIV, and the PCC of each STHSPM algorithm is also given in the two tables. Similar to the conclusion drawn from visual comparison, the accuracy of ICK is found to be the highest among five STHSPM algorithms at each scale. ICK generates significantly higher accuracies than the other four STHSPM algorithms in all cases. The reason is attributed to the fact that the geostatistics-based ICK method extracts prior spatial structure information of each class from additional fine spatial resolution images. Therefore, ICK is advantageous while dealing with complex spatial patterns.

compared visually and quantitatively. As the effectiveness and advantages of the proposed UOC have been demonstrated by three experiments, we compare the results of five STHSPM algorithms when UOC is applied in class allocation, with visiting order of classes specified by Moran's I that was estimated from coarse fraction images.

For visual comparison, we focus on the results in the second experiment (i.e., the last column in Fig. 12). It can be seen that

TABLE XIII
MCNEMAR'S TEST FOR STHSPM ALGORITHMS IN EXPERIMENT 1

| | S=5 | | | | | S=10 | | | | |
	BPNN 91.58%	HNN 94.19%	SPSAM 93.79%	Kriging 93.89%	ICK 94.51%	BPNN 84.60%	HNN 85.43%	SPSAM 88.90%	Kriging 88.90%	ICK 89.33%
BPNN		21.1843	18.0989	19.0711	23.7284		6.3056	34.6841	35.0997	38.5479
HNN			-4.8908	-3.7968	4.8900			31.3589	35.4653	42.1081
SPSAM				1.2009	8.2348				0.1069	4.9997
Kriging					7.8360					5.8163
ICK										

TABLE XIV
MCNEMAR'S TEST FOR STHSPM ALGORITHMS IN EXPERIMENT 2

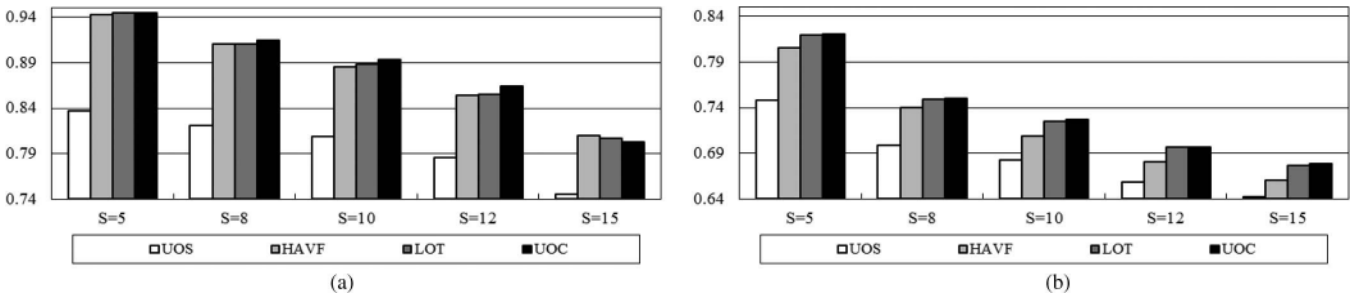| | S=8 | | | | | S=12 | | | | |
	BPNN 69.58%	HNN 73.00%	SPSAM 74.14%	Kriging 74.50%	ICK 75.05%	BPNN 65.10%	HNN 67.31%	SPSAM 68.30%	Kriging 69.10%	ICK 69.72%
BPNN		21.6263	29.0998	31.2864	34.9863		13.6655	19.9154	25.1336	28.8840
HNN			8.9742	13.0703	19.1045			7.6262	15.3039	21.1230
SPSAM				3.6298	7.9308				8.5525	12.5661
Kriging					5.9101					7.0524
ICK										

Fig. 17. PCC of ICK combined with different class allocation methods for various scale factor S. (a) Land cover map of Bath, U.K., in experiment 1. (b) Land cover map of Nanjing, China, in experiment 2.

However, for another learning-based SPM method, i.e., BPNN, it does not obtain satisfactory accuracies, which indicates that BPNN still needs an additional training data set [53]. As for the three STHSPM algorithms that need no prior spatial structure information, HNN gives the highest accuracy at small scale $S = 5$ in experiment 1, whereas kriging is advantageous at large scales. In HNN, the spatial dependence is expressed at the subpixel scale level and the spatial relation between subpixel, and its nearest eight neighboring subpixels are considered. On the one hand, this character enables HNN to produce more continuous and better SPM results at small scale than do SP-SAM and kriging that consider dependence between subpixel and its neighboring coarse pixel. On the other hand, due to this character of HNN, spatial locations of subpixels for each class vary after each mapping, and iterations are needed to acquire SPM results. It is easy to fall into local optimum, particularly for complex SPM problems at large zoom scales. This is similar to the case in pixel swapping algorithm [10], [11], [14], which also considers dependence at the subpixel scale level. Consequently, kriging could be a promising SPM approach for the large-scale situation when prior spatial structure information is unavailable.

F. Analysis of Scale Factor S

Here, scale factor S is analyzed for UOS, HAVF, LOT, and UOC. The bar charts of PCC with various scales are shown in Fig. 17 for the land cover maps in the first and second experiments. The four class allocation methods were applied to the STHSPM algorithm ICK. In the bar charts, the PCC of UOS is the average of 100 random runs. The visiting order for UOC is determined by Moran's I, which was calculated from fraction images. Five scales, i.e., 5, 8, 10, 12, and 15, were discussed for each land cover map.

Due to the complex land cover pattern in the map of Nanjing, the SPM accuracy of each method in Fig. 17(b) is much lower than that in Fig. 17(a). Precisely, for the same scale, the PCC of each method in Fig. 17(b) is at least 12% lower than that in Fig. 17(a). As the scale increases, the PCC of all class allocation methods in the two subfigures takes on the tendency

TABLE XV
McNemar's Test for Results in Fig. 17 (0: UOC; 1: UOS; 2: HAVF; 3: LOT)

S	Land cover map of Bath			Land cover map of Nanjing		
	z_{01}	z_{02}	z_{03}	z_{01}	z_{02}	z_{03}
5	[59.8257, 62.3790]	7.8893	4.3911	[45.0977, 47.8272]	18.4676	*1.7748*
8	[63.8370, 66.5983]	13.4000	12.4416	[35.2192, 37.9695]	21.1905	*1.9010*
10	[63.2382, 65.4879]	21.0428	16.8453	[31.5941, 34.5169]	18.7045	2.0944
12	[59.9077, 62.2882]	21.8308	22.1929	[27.8429, 30.7404]	16.9686	*1.2814*
15	[44.0706, 47.3966]	-10.5289	-8.0895	[26.5480, 28.9816]	17.5462	2.6954

of descension. Furthermore, compared with the other three class allocation methods, the proposed UOC achieve higher SPM accuracy for nearly all scales. The McNemar's test results in Table XV indicate that UOC generates significantly different results, in comparison with UOS and HAVF, for both land cover maps. The difference between UOC and LOT is significant for the land cover map of Bath, but becomes insignificant for $S = 5$, 8, and 12 for the land cover map of Nanjing. We can find that the spatial dependence of the land cover in the map of Bath is stronger than that in the map of Nanjing. Hence, the difference between UOC and LOT illustrates that UOC is more advantageous when the spatial autocorrelation in the studied area is stronger.

VI. CONCLUSION

This paper has presented a novel class allocation method UOC for STHSPM algorithms. The STHSPM algorithm first obtains the soft-classified images for each land cover class at target fine spatial resolution and then allocates classes for each fine pixel according to the soft attribute values and constraints from class fractions. With the UOC-based class allocation method, subpixels for each class are allocated in turn. The visiting order of classes can be specified by Moran's I, which can be estimated from either an available high spatial resolution land cover map or coarse fraction images. UOC has the unique advantage of taking account of the intraclass spatial correlation in the second step of STHSPM algorithms. In the experiments on three remote sensing images, the proposed UOC was applied to five STHSPM algorithms, i.e., BPNN, HNN, SPSAM, kriging, and ICK, and compared with the existing class allocation methods, i.e., UOS, HAVF, and LOT. The conclusions are summarized as follows.

1) The visiting order of classes in UOC can be reasonably determined by comparing Moran's I of each class. When spatial structure information of classes at fine spatial resolution is available, they can be readily utilized for calculating Moran's I of classes. However, when such prior information is unavailable, our proposed method that uses fraction images to calculate Moran's I can also select out a reasonable order.

2) UOC was successfully applied to five STHSPM algorithms. For all five STHSPM algorithms, with Moran's I that was estimated from fraction images, UOC is capable of obtaining more accurate SPM results than UOS and HAVF and achieving at least comparable SPM accuracy in comparison with LOT. When the intraclass spatial correlation in the studied area is stronger, the advantage of UOC in terms of SPM accuracy, particularly over LOT, is more obvious. This is because UOC considers the intraclass spatial dependence in the second step of STHSPM algorithms.

3) Similar to UOS and HAVF, the computing complexity of UOC is much less than that of LOT. Therefore, UOC shows its great potential in real-time applications.

4) The intercomparison of five STHSPM algorithms reveals that ICK is able to obtain the highest SPM accuracy among the five algorithms, which is based on the proposed UOC with Moran's I estimated from fraction images. However, this advantage of ICK is based on the existence of prior spatial structure information of land cover that is representative of the studied area.

In the fields of image and signal processing, there are many available superresolution reconstruction algorithms, such as image interpolation, maximum *a posteriori*, iterative backward projection, projection onto convex sets, etc. These algorithms are also capable of obtaining the soft-classified image per class at fine spatial resolution when coarse fraction images are used as input. The proposed UOC can be used to harden these soft-classified images and generate SPM results. Therefore, UOC builds a bridge between superresolution reconstruction and SPM. This seems to be considerably promising, and our future work will focus on it.

REFERENCES

[1] G. M. Foody, "Status of land cover classification accuracy assessment," *Remote Sens. Environ.*, vol. 80, no. 1, pp. 185–201, Apr. 2002.

[2] A. Plaza, P. Martinez, R. Perez, and J. Plaza, "A quantitative and comparative analysis of endmember extraction algorithms from hyperspectral data," *IEEE Trans. Geosci. Remote Sens.*, vol. 42, no. 3, pp. 650–663, Mar. 2004.

[3] L. Wang and X. Jia, "Integration of soft and hard classification using extended support vector machine," *IEEE Geosci. Remote Sens. Lett.*, vol. 6, no. 3, pp. 543–547, Jul. 2009.

[4] P. M. Atkinson, "Mapping sub-pixel boundaries from remotely sensed images," in *Innovations in GIS*. New York, NY, USA: Taylor & Francis, 1997, pp. 166–180.

[5] T. Kasetkasem, M. K. Arora, and P. K. Varshney, "Super-resolution land-cover mapping using a Markov random field based approach," *Remote Sens. Environ.*, vol. 96, no. 3/4, pp. 302–314, Jun. 2005.

[6] V. A. Tolpekin and A. Stein, "Quantification of the effects of land-cover-class spectral separability on the accuracy of Markov-random-field based superresolution mapping," *IEEE Trans. Geosci. Remote Sens.*, vol. 47, no. 9, pp. 3283–3297, Sep. 2009.

[7] Q. Wang, L. Wang, and D. Liu, "Particle swarm optimization-based sub-pixel mapping for remote-sensing imagery," *Int. J. Remote Sens.*, vol. 33, no. 20, pp. 6480–6496, Oct. 2012.

[8] Q. Wang, L. Wang, and D. Liu, "Integration of spatial attractions between and within pixels for sub-pixel mapping," *J. Syst. Eng. Electron.*, vol. 23, no. 2, pp. 293–303, Apr. 2012.

[9] Z. Shen, J. Qi, and K. Wang, "Modification of pixel-swapping algorithm with initialization from a sub-pixel/pixel spatial attraction model," *Photogramm. Eng. Remote Sens.*, vol. 75, no. 5, pp. 557–567, May 2009.

[10] P. M. Atkinson, "Sub-pixel target mapping from soft-classified, remotely sensed imagery," *Photogramm. Eng. Remote Sens.*, vol. 71, no. 7, pp. 839–846, Jul. 2005.

[11] Y. Makido and A. Shortridge, "Weighting function alternatives for a sub-pixel allocation model," *Photogramm. Eng. Remote Sens.*, vol. 73, no. 11, pp. 1233–1240, Nov. 2007.

[12] K. C. Mertens, L. P. C. Verbeke, E. I. Ducheyne, and R. De Wulf, "Using genetic algorithms in sub-pixel mapping," *Int. J. Remote Sens.*, vol. 24, no. 21, pp. 4241–4247, Nov. 2003.

[13] F. Ling, W. Li, Y. Du, and X. Li, "Land cover change mapping at the subpixel scale with different spatial-resolution remotely sensed imagery," *IEEE Geosci. Remote Sens. Lett.*, vol. 8, no. 1, pp. 182–186, Jan. 2011.

[14] Y. Makido, A. Shortridge, and J. P. Messina, "Assessing alternatives for modeling the spatial distribution of multiple land-cover classes at sub-pixel scales," *Photogramm. Eng. Remote Sens.*, vol. 73, no. 8, pp. 935–943, Aug. 2007.

[15] A. Villa, J. Chanussot, J. A. Benediktsson, and C. Jutten, "Spectral unmixing for the classification of hyperspectral images at a finer spatial resolution," *IEEE J. Sel. Topics Signal Process.*, vol. 5, no. 3, pp. 521–533, Jun. 2011.

[16] P. M. Atkinson, "Super-resolution mapping using the two-point histogram and multi-source imagery," in *Proc. GeoENV VI*, 2008, pp. 307–321.

[17] A. M. Muslim, G. M. Foody, and P. M. Atkinson, "Shoreline mapping from coarse-spatial resolution remote sensing imagery of Seberang Takir, Malaysia," *J. Coastal Res.*, vol. 23, no. 6, pp. 1399–1408, Nov. 2007.

[18] H. Lin, Y. Bo, J. Wang, and X. Jia, "Landscape structure based super-resolution mapping from remotely sensed imagery," in *Proc. Int. Geosci. Remote Sens. Symp.*, 2011, pp. 79–82.

[19] K. C. Mertens, L. P. C. Verbeke, T. Westra, and R. De Wulf, "Sub-pixel mapping and sub-pixel sharpening using neural network predicted wavelet coefficients," *Remote Sens. Environ.*, vol. 91, no. 2, pp. 225–236, May 2004.

[20] K. C. Mertens, B. D. Basets, L. P. C. Verbeke, and R. De Wulf, "A sub-pixel mapping algorithm based on sub-pixel/pixel spatial attraction models," *Int. J. Remote Sens.*, vol. 27, no. 15, pp. 3293–3310, Aug. 2006.

[21] K. C. Mertens, L. P. C. Verbeke, and R. DeWulf, "Sub-pixel mapping with neural networks: Real-world spatial configurations learned from artificial shapes," in *Proc. 4th Int. Symp. Remote Sens. Urban Areas*, Regensburg, Germany, 2003, pp. 117–121.

[22] L. Wang, Y. Zhang, and J. Li, "BP neural network based sub-pixel mapping method," in *Proc. Int. Conf. Intell. Comput.*, 2006, pp. 755–760.

[23] D. Nigussie, R. Zurita-Milla, and J. G. P. W. Clevers, "Possibilities and limitations of artificial neural networks for subpixel mapping of land cover," *Int. J. Remote Sens.*, vol. 32, no. 22, pp. 7203–7226, Nov. 2011.

[24] A. J. Tatem, H. G. Lewis, P. M. Atkinson, and M. S. Nixon, "Super-resolution target identification from remotely sensed images using a Hopfield neural network," *IEEE Trans. Geosci. Remote Sens.*, vol. 39, no. 4, pp. 781–796, Apr. 2001.

[25] A. J. Tatem, H. G. Lewis, P. M. Atkinson, and M. S. Nixon, "Multiclass land cover mapping at the sub-pixel scale using a Hopfield neural network," *Int. J. Appl. Earth Observ. Geoinform.*, vol. 3, no. 2, pp. 184–190, 2001.

[26] A. J. Tatem, H. G. Lewis, P. M. Atkinson, and M. S. Nixon, "Increasing the spatial resolution of agricultural land cover maps using a Hopfield neural network," *Int. J. Geograph. Inf. Sci.*, vol. 17, no. 7, pp. 647–672, 2003.

[27] A. M. Muad and G. M. Foody, "Impact of land cover patch size on the accuracy of patch area representation in HNN-based super resolution

[28] J. Verhoeye and R. De Wulf, "Land-cover mapping at sub-pixel scales using linear optimization techniques," *Remote Sens. Environ.*, vol. 79, no. 1, pp. 96–104, Jan. 2002.

[29] A. Boucher and P. C. Kyriakidis, "Super-resolution land cover mapping with indicator geostatistics," *Remote Sens. Environ.*, vol. 104, no. 3, pp. 264–282, Oct. 2006.

[30] A. Boucher, P. C. Kyriakidis, and C. Cronkite-Ratcliff, "Geostatistical solutions for super-resolution land cover mapping," *IEEE Trans. Geosci. Remote Sens.*, vol. 46, no. 1, pp. 272–283, Jan. 2008.

[31] A. Boucher, "Sub-pixel mapping of coarse satellite remote sensing images with stochastic simulations from training images," *Math. Geosci.*, vol. 41, no. 3, pp. 265–290, Apr. 2009.

[32] H. Jin, G. Mountrakis, and P. Li, "A super-resolution mapping method using local indicator variograms," *Int. J. Remote Sens.*, vol. 33, no. 24, pp. 7747–7773, Dec. 2012.

[33] G. M. Foody, A. M. Muslim, and P. M. Atkinson, "Super-resolution mapping of the waterline from remotely sensed data," *Int. J. Remote Sens.*, vol. 26, no. 24, pp. 5381–5392, Dec. 2005.

[34] Y. F. Su, G. M. Foody, A. M. Muad, and K. S. Cheng, "Combining pixel swapping and contouring methods to enhance super-resolution mapping," *IEEE J. Sel. Topics Appl. Earth Observ. Remote Sens.*, vol. 5, no. 5, pp. 1428–1437, Oct. 2012.

[35] Y. Ge, S. Li, and V. C. Lakhan, "Development and testing of a subpixel mapping algorithm," *IEEE Trans. Geosci. Remote Sens.*, vol. 47, no. 7, pp. 2155–2164, Jul. 2009.

[36] J. P. Ardila, V. A. Tolpekin, W. Bijker, and A. Stein, "Markov-random-field-based super-resolution mapping for identification of urban trees in VHR images," *ISPRS J. Photogramm. Remote Sens.*, vol. 66, no. 6, pp. 762–775, Nov. 2011.

[37] X. Li, F. Ling, and Y. Du, "Super-resolution mapping based on the supervised fuzzy c-means approach," *Remote Sens. Lett.*, vol. 3, no. 6, pp. 501–510, Nov. 2012.

[38] M. Q. Nguyen, P. M. Atkinson, and H. G. Lewis, "Superresolution mapping using a Hopfield neural network with LIDAR data," *IEEE Geosci. Remote Sens. Lett.*, vol. 2, no. 3, pp. 366–370, Jul. 2005.

[39] M. Q. Nguyen, P. M. Atkinson, and H. G. Lewis, "Superresolution mapping using a Hopfield neural network with fused images," *IEEE Trans. Geosci. Remote Sens.*, vol. 44, no. 3, pp. 736–749, Mar. 2006.

[40] F. Ling, Y. Du, F. Xiao, H. Xue, and S. Wu, "Super-resolution land-cover mapping using multiple sub-pixel shifted remotely sensed images," *Int. J. Remote Sens.*, vol. 31, no. 19, pp. 5023–5040, Oct. 2010.

[41] A. M. Muad and G. M. Foody, "Super-resolution mapping of lakes from imagery with a coarse spatial and fine temporal resolution," *Int. J. Appl. Earth Observ. Geoinform.*, vol. 15, pp. 79–91, Apr. 2012.

[42] M. Q. Nguyen, P. M. Atkinson, and H. G. Lewis, "Super-resolution mapping using Hopfield neural network with panchromatic imagery," *Int. J. Remote Sens.*, vol. 32, no. 21, pp. 6149–6176, Nov. 2011.

[43] A. Boucher and P. C. Kyriakidis, "Integrating fine scale information in super-resolution land-cover mapping," *Photogramm. Eng. Remote Sens.*, vol. 73, no. 8, pp. 913–921, Aug. 2007.

[44] F. Ling, F. Xiao, Y. Du, H. Xue, and X. Ren, "Waterline mapping at the subpixel scale from remote sensing imagery with high-resolution digital elevation models," *Int. J. Remote Sens.*, vol. 29, no. 6, pp. 1809–1815, Mar. 2008.

[45] M. W. Thornton, P. M. Atkinson, and D. A. Holland, "A linearised pixel-swapping method for mapping rural linear land cover features from fine spatial resolution remotely sensed imagery," *Comput. Geosci.*, vol. 33, no. 10, pp. 1261–1272, Oct. 2007.

[46] P. M. Atkinson, "Issues of uncertainty in super-resolution mapping and their implications for the design of an inter-comparison study," *Int. J. Remote Sens.*, vol. 30, no. 20, pp. 5293–5308, Oct. 2009.

[47] P. Goovaerts, *Geostatistics for Natural Resources Evaluation*. London, U.K.: Oxford Univ. Press, 1997.

[48] B. Kolman and R. E. Beck, *Elementary Linear Programming With Applications*. New York, NY, USA: Academic, 1995.

[49] L. Wang and Q. Wang, "Subpixel mapping using Markov random field with multiple spectral constraints from subpixel shifted remote sensing images," *IEEE Geosci. Remote Sens. Lett.*, vol. 10, no. 3, pp. 598–602, May 2013.

[50] X. Xu, Y. Zhong, and L. Zhang, "Adaptive sub-pixel mapping based on a multi-agent system for remote sensing imagery," *IEEE Trans. Geosci. Remote Sens.*, vol. 52, no. 2, pp. 787–804, Feb. 2014.

[51] G. M. Foody, "Thematic map comparison evaluating the statistical significance of differences in classification accuracy," *Photogramm. Eng. Remote Sens.*, vol. 70, no. 5, pp. 627–633, May 2004.

[52] A. J. Tatem, H. G. Lewis, P. M. Atkinson, and M. S. Nixon, "Super-resolution mapping of urban scenes from IKONOS imagery using a Hopfield neural network," in *Proc. Int. Geosci. Remote Sens. Symp.*, Sydney, Australia, 2001, pp. 3200–3205.

[53] Y. Zhong and L. Zhang, "Remote sensing image subpixel mapping based on adaptive differential evolution," *IEEE Trans. Syst., Man, Cybern. B, Cybern.*, vol. 42, no. 5, pp. 1306–1329, Oct. 2012.

[54] Y. Zhong and L. Zhang, "Sub-pixel mapping based on artificial immune systems for remote sensing imagery," *Pattern Recognit.*, vol. 46, no. 11, pp. 2902–2926, Nov. 2013.

[55] [Online]. Available: http://www.ceode.cas.cn/txzs/dxyy/

[56] D. C. Heinz and C.-I. Chang, "Fully constrained least squares linear spectral mixture analysis method for material quantification in hyperspectral imagery," *IEEE Trans. Geosci. Remote Sens.*, vol. 39, no. 3, pp. 529–545, Mar. 2001.

[57] X. Xu, Y. Zhong, L. Zhang, and H. Zhang, "Sub-pixel mapping based on a MAP model with multiple shifted hyperspectral imagery," *IEEE J. Sel. Topics Appl. Earth Observ. Remote Sens.*, vol. 6, no. 2, pp. 580–593, Apr. 2013.

[58] Y. Ge, "Sub-pixel land-cover mapping with improved fraction images upon multiple-point simulation," *Int. J. Appl. Earth Observ. Geoinform.*, vol. 22, pp. 115–126, Jun. 2013.

Wenzhong Shi received the Ph.D. degree from the University of Osnabrück, Vechta, Germany, in 1994.

He is a Professor in GIS and remote sensing with the Department of Land Surveying and Geo-Informatics, The Hong Kong Polytechnic University, Kowloon, Hong Kong. He is also with Wuhan University, Wuhan, China. His current research interests include GIS and remote sensing, uncertainty and spatial data quality control, and image processing for high-resolution satellite images. He has published about 400 research articles (including over 80 SCI papers) and ten books.

Prof. Shi was a recipient of the State Natural Science Award from the State Council of China in 2007.

Qunming Wang received the B.S. and M.S. degrees from Harbin Engineering University, Harbin, China, in 2010 and 2012, respectively. He is currently working toward the Ph.D. degree in the Department of Land Surveying and Geo-Informatics, The Hong Kong Polytechnic University, Kowloon, Hong Kong.

His current research interests focus on remote sensing image analysis and pattern recognition.

Mr. Wang was a recipient of the Excellent Master Dissertation Award and the Excellent Graduates in Heilongjiang, China, in 2012. He has been awarded the hyper-competitive Hong Kong Ph.D. Fellowship. He serves as a Reviewer for IEEE TRANSACTIONS ON GEOSCIENCE and REMOTE SENSING, IEEE GEOSCIENCE and REMOTE SENSING LETTERS, IEEE JOURNAL OF SELECTED TOPICS IN APPLIED EARTH OBSERVATION AND REMOTE SENSING, and the *International Journal of Remote Sensing*.

Liguo Wang received the M.S. degree and Ph.D. degree in signal and information processing from Harbin Institute of Technology, Harbin, China, in 2002 and 2005, respectively.

From 2006 to 2008, he was a Postdoctoral Researcher with the Center of Information and Communications Engineering, Harbin Engineering University, Harbin, where he is currently a Professor. His research interests include remote sensing and machine learning. He has published one book titled *Processing Techniques of Hyperspectral Imagery* (Nat. Defence Industry Press, 2013) and more than 80 papers in journals and conference proceedings.